TURUN
YLIOPISTO
UNIVERSITY
OF TURKU

OXIDATIVE MULTILAYER FILMS AND EUMELANIN ANALOGS FOR BIOCOMPATIBLE SUPERCAPACITORS

Lauri Marttila

TURUN YLIOPISTON JULKAISUJA – ANNALES UNIVERSITATIS TURKUENSIS
SARJA – SER. AI OSA – TOM. 681 | ASTRONOMICA – CHEMICA – PHYSICA – MATHEMATICA | TURKU 2022

TURUN
YLIOPISTO
UNIVERSITY
OF TURKU

OXIDATIVE MULTILAYER FILMS AND EUMELANIN ANALOGS FOR BIOCOMPATIBLE SUPERCAPACITORS

Lauri Marttila

TURUN YLIOPISTON JULKAISUJA – ANNALES UNIVERSITATIS TURKUENSIS
SARJA – SER. AI OSA – TOM. 681 | ASTRONOMICA - CHEMICA - PHYSICA – MATHEMATICA | TURKU 2022

University of Turku

Faculty of Science
Department of Chemistry
Chemistry
Doctoral Programme in Exact Sciences

Supervised by

Professor, Jukka Lukkari
Department of Chemistry
University of Turku
Turku, Finland

University Teacher, Henri Kivelä
Department of Chemistry
University of Turku
Turku, Finland

Adjunct Professor, Mikko Salomäki
Department of Chemistry
University of Turku
Turku, Finland

Reviewed by

Doctor, Klemen Pirnat
Department of Materials Chemistry
National Institute of Chemistry
Ljubljana, Slovenia

Professor, Tomi Laurila
Department of Electrical Engineering
and Automation
Aalto University
Espoo, Finland

Opponent

Associate Professor,
Radosław Mrówczyński
Faculty of Chemistry
Adam Mickiewicz University
Poznań, Poland

The originality of this publication has been checked in accordance with the University of Turku quality assurance system using the Turnitin OriginalityCheck service.

ISBN 978-951-29-9095-5 (PRINT)
ISBN 978-951-29-9096-2 (PDF)
ISSN 0082-7002 (Print)
ISSN 2343-3175 (Online)
Painosalama, Turku, Finland 2022

UNIVERSITY OF TURKU
Faculty of Science
Department of Chemistry
Chemistry
LAURI MARTTILA: Oxidative Multilayer Films and Eumelanin Analogs for Biocompatible Supercapacitors
Doctoral Dissertation, 277 pp.
Doctoral Programme in Exact Sciences (EXACTUS)
December 2022

ABSTRACT

The future applications of implantable electronic medical devices set heavy requirements for the materials powering the devices. They need to be biocompatible or even biodegradable and have sufficient electrochemical properties. The primary goal of this work was to provide knowledge on materials that can be potentially used as electrode materials in biocompatible and/or biodegradable supercapacitors.

The first material of interest was eumelanin, pigment found e.g. in the human skin. We studied synthetic eumelanin analogs polydopamine (from dopamine) and DHI-melanin (from 5,6-dihydroxyindole (DHI)). Dopamine has multiple oxidation routes and we focused on the critical initial steps in the Raper-Mason pathway, which leads to the DHI-melanin-like compound. We studied the pH dependence of the dopamine oxidation in two cases: (1) oxidation by O_2 only, and (2) oxidation in the presence of Ce(IV), Fe(III) or Cu(II) ion. Secondly, we oxidized DHI to DHI-melanin directly on top of the oxidative film and analyzed its chemical composition in detail.

As a second topic, we studied the oxidative layer-by-layer (LbL) films composed of polyphosphate (PP), graphene oxide (GO) and Ce(IV)/Ce(III) ions: $(PP/Ce/GO/Ce)_n$. Ce(IV) ions in these films can oxidize monomers from their surrounding solution onto the film structure. In this work, we prepared oxidative films with advanced spin-spray LbL method. Build-up time of the films was much faster compared with the traditional dip-LbL method, the films were smoother, they had a stratified structure, and their thickness could be controlled with high precision.

Oxidative films can be used to prepare thin electroactive GO/PEDOT films with ca. 80 % w/w biocompatible conducting polymer PEDOT. These films have promising charge transfer kinetics and ca. 100 F/cm^3 capacitance. By using electrochemical impedance and capacitance spectroscopies, we demonstrated that the main contribution to the capacitance comes from redox processes. $(PP/Ce/rGO/Ce)_{15}$/(DHI-melanin) film had even higher capacitance. However, the results emphasize that DHI-melanin must be mixed with more electronically conductive materials to improve its dynamic properties.

TURUN YLIOPISTO
Matemaattis-luonnontieteellinen tiedekunta
Kemian laitos
Kemia
LAURI MARTTILA: Hapettavat monikerroskalvot ja eumelaniinianalogit materiaaleina bioyhteensopivissa superkondensaattoreissa
Väitöskirja, 277 s.
Eksaktien tieteiden tohtoriohjelma (EXACTUS)
Joulukuu 2022

TIIVISTELMÄ

Bioyhteensopivien tai jopa biohajoavien elektronisten lääketieteellisten laitteiden kehittäminen asettaa korkeat vaatimukset materiaaleille, joista laitteet saavat virtaa. Tämän työn päätavoitteena oli tuottaa tietoa materiaaleista, joita voidaan potentiaalisesti käyttää elektrodimateriaaleina bioyhteensopivissa ja/tai biohajoavissa superkondensaattoreissa.

Olemme erityisen kiinnostuneita eumelaniinista, jota on pigmenttinä esimerkiksi ihmisen ihossa. Tutkimme synteettisiä eumelaniinianalogeja, polydopamiinia ja DHI-melaniinia, joita valmistetaan dopamiinista ja 5,6-dihydroksi-indolista (DHI). Dopamiinilla on useita hapettumisreittejä ja me keskityimme kriittisiin ensiaskeleisiin Raper-Mason-reaktioreitissä, joka johtaa DHI-melaniinin kaltaiseen yhdisteeseen. Tutkimme dopamiinin hapettumisen pH-riippuvuutta kahdessa tapauksessa: (1) hapettimena vain O_2 ja (2) hapettuminen Ce(IV)-, Fe(III)- tai Cu(II)-ionin läsnäollessa. Hapetimme myös DHI:a DHI-melaniiniksi suoraan hapettavan kalvon pinnalle ja analysoimme sen kemiallista koostumusta yksityiskohtaisesti.

Tutkimme myös hapettavia kerros-kerrokselta (LbL) kalvoja, jotka koostuvat polyfosfaatista (PP), grafeenioksidista (GO) ja Ce(IV)/Ce(III)-ioneista: $(PP/Ce/GO/Ce)_n$. Kalvoissa olevat Ce(IV)-ionit voivat hapettaa monomeerejä ympäröivästä liuoksesta kalvon rakenteeseen. Väitöskirjatyössäni valmistimme hapettavia kalvoja kehittyneellä ruiskutuspyöritys-LbL-menetelmällä. Näiden kalvojen kerrostusaika on paljon nopeampi verrattuna perinteiseen kastomenetelmään. Lisäksi kalvot ovat paljon tasaisempia, niillä on kerrostunut rakenne ja niiden paksuutta voidaan kontrolloida hyvin tarkasti.

Hapettavia kalvoja voidaan käyttää ohuiden, sähkökemiallisesti aktiivisten GO/PEDOT-kalvojen valmistukseen, joissa on noin 80 % w/w bioyhteensopivaa PEDOT-johdepolymeeriä. Näillä kalvoilla on lupaava varauksensiirtokinetiikka ja noin 100 F/cm^3 kapasitanssi. Havaitsimme sähkökemiallisesta impedanssispektroskopiasta johdetulla kapasitanssispektroskopialla, että suurin osa kalvojen kapasitanssista on peräisin redoksiprosesseista. $(PP/Ce/rGO/Ce)_{15}$/DHI-melaniinikalvolla oli vielä suurempi kapasitanssi. Tulokset kuitenkin korostivat, että DHI-melaniinia on seostettava paremmin elektronisesti johtavien materiaalien kanssa sen dynaamisten ominaisuuksien parantamiseksi.

Table of Contents

Abbreviations

(a1/a2/.../ax)n	Multilayer with n (a1/a2/.../ax) layers, e.g. (PP/Ce/GO/Ce)n
AFM	Atomic force microscopy
Ag/AgCl	Silver/silver chloride reference electrode
CV	Cyclic voltammetry
DA	Dopamine
DAC	Dopaminechrome
DAL	Leucodopaminechrome
DFT	Density functional theory
DHI	5,6-Dihydroxyindole
DHICA	5,6-dihydroxyindole-2-carboxylic acid
DHQ	Dopaminehydroquinone
DQ	Dopaminequinone
DSQ	Dopaminesemiquinone
EDLC	Electrochemical double-layer capacitor
EDOT	3,4-ethylenedioxythiophene
EDS	Energy dispersive X-ray spectroscopy analysis
EIS	Electrochemical impedance spectroscopy
GO	Graphene oxide
HP	Hydrogen peroxide
H2Q	Hydroquinone
IQ	5,6-Indolequinone
LbL	Layer-by-layer
LPDP	Liquid phase depositional polymerization
NMR	Nuclear magnetic resonance spectroscopy
oCVD	Oxidative chemical vapor deposition
PAH	Poly(allylamine hydrochloride)
PDCA	Pyrrole-2,3-dicarboxylic acid
PEDOT	Poly(3,4-ethylenedioxythiophene)
PP	Polyphosphate
PSS	Polystyrene sulfonate
Q	Quinone

QM	Quinone methide
rGO	Reduced graphene oxide
(r)GO	Graphene oxide or reduced graphene oxide
SEM	Scanning electron microscopy
SO	Superoxide
SQ	Semiquinone
SWLI	Scanning white light interferometry
UV-Vis	Ultraviolet-visible
VPP	Vapor phase polymerization
XPS	X-ray photoelectron spectroscopy

List of Included Original Publications

The experimental part of this thesis is based on the following original publications, which are referred to in the text by their Roman numerals:

I Salomäki, M.; Marttila, L.; Kivelä, H.; Ouvinen, T.; Lukkari, J. Effects of pH and Oxidants on the First Steps of Polydopamine Formation: A Thermodynamic Approach. *J. Phys. Chem. B*, 2018; 24: 6314–6327. https://doi.org/10.1021/acs.jpcb.8b02304

II Salomäki, M.; Marttila, L.; Kivelä, H.; Tupala, M.; Lukkari, J. Oxidative Spin-Spray-Assembled Coordinative Multilayers as Platforms for Capacitive Films. *Langmuir*, 2020; 24: 6736–6748. https://doi.org/10.1021/acs.langmuir.0c00824

III Marttila, L.; Salomäki, M.; Kivelä, H.; Hassinen, J.; Granroth, S.; Mäkilä, E.; Nyman, J.; Lukkari, J. Effect of Monomers and Deposition Conditions on Capacitive Polymer Films Prepared Using Oxidative Multilayers. Submitted.

Doctoral candidate's role under the following themes in each publication:
Research design I: Practical detailed research design during the laboratory work. **II:** Suggestions for research design, and practical detailed research design during the laboratory work. **III:** Participation in research design.
Practical/laboratory work I: Most of the experimental work. **II:** Practically all experimental work. **III:** All experimental work except NMR, SEM-EDS, and light interferometry.
Data processing I: Participation in data processing. **II:** Most of the data processing. **III:** Most of the data processing except NMR, kinetic modelling, and light interferometry.
Writing of the manuscript I: Participation in writing of the manuscript. **II:** Coauthoring of the manuscript. **III:** Principal author.

List of Other Related Publications

Salomäki, M.; Ouvinen, T.; Marttila, L.; Kivelä, H.; Leiro, J.; Mäkilä, E.; Lukkari, J. Polydopamine Nanoparticles Prepared Using Redox-Active Transition Metals. *J. Phys. Chem. B*, 2019; 11: 2513–2524. https://doi.org/10.1021/acs.jpcb.8b11994

1 Introduction

Our everyday lives are full of electronical devices that increase our standard of living. As a downside, 53.6 million tons of electronic waste was produced in 2019 and the amount is projected to grow sharply.[1] Less than one-fifth of this waste was documented as properly collected and recycled.[1]

Electronical devices are typically designed for long-lifetime operation, but recent reviews show that there is a large interest towards biocompatible and even biodegradable electronic materials and devices.[2–7] Biodegradable electronics could be used in many special applications such as environmental monitors, consumer electronics and data-secure hardware,[2] easing the electronic waste management problem and opening possibilities for the large-scale environmental analysis. Additionally, ideal transient implantable medical devices would be safely absorbed by the body after their intended lifetime, which would decrease the risk of infection and eliminate the need for surgery for device retrieval.[2,3]

The heart of an electronical device is its power source. However, as it has been reviewed recently,[2,4–7] the development of biocompatible and biodegradable power sources is still an emerging technology. The materials development for these devices is not an easy task since they need to be nontoxic, biocompatible, and biodegradable, have appropriate mechanical properties such as sufficient flexibility, and still have high-quality electrochemical performance.[5]

In this thesis, I will discuss three main topics relevant to the development of active energy storage materials for supercapacitors. First, I will discuss two interesting energy storage materials for the power sources: classical conducting polymer poly(3,4-ethylenedioxythiophene) (PEDOT) and natural pigment eumelanin and its synthetic analogues (both are hereby referred as eumelanins or melanins for simplicity unless otherwise specified). The conducting polymer PEDOT is not biodegradable, but it is biocompatible.[8–10] Its composites have high potential in supercapacitors powering wearable health monitoring devices[11–14] and even implantable bioelectronics[15]. Melanin, on the other hand, is both biocompatible and biodegradable,[16,17] and its potential as an energy storage material in both batteries[18–22] and supercapacitors[23–27] has been demonstrated in the literature.

The formation reactions of PEDOT and eumelanins are both complex oxidative polymerization processes,[28–30] and, as a consequence, properties of them and their composites naturally vary according to the chosen fabrication method. Thus, as a third main topic in the thesis, I introduce the relatively little studied method for the fabrication of electroactive films: oxidative multilayers. These layer-by-layer (LbL) films can oxidize EDOT or 5,6-dihydroxyindole (DHI) monomers from ambient directly onto the multilayer structure (to PEDOT or DHI-melanin respectively) and thus represent a general technology platform for the fabrication of electroactive films [**articles II, III]**. Polydopamine is chemically similar to DHI-melanin when it is formed by the oxidation of dopamine under suitable conditions.[31] Therefore, we also studied the polydopamine formation reaction in detail.[**article I**]

The more specific main aims of this thesis are twofold.

- To develop the method of electroactive film fabrication by oxidative films. I studied the fabrication of the oxidative films by spin-spray layer-by-layer assembly method. As a model system for electroactive films, I polymerized PEDOT onto the oxidative films and studied especially the composition and electrochemical properties of the films.
- To study the preparation of synthetic eumelanin analogues polydopamine and DHI-melanin. First, I studied the critical first steps in the oxidation of dopamine to 5,6-dihydroxyindole and further to polydopamine. Second, I oxidized DHI to DHI-melanin onto the oxidative films, studied its chemical composition and showed that the film is electroactive with promising electrochemical properties worthy of further studies.

Our primary research questions can be formulated as follows: 1) can the oxidative multilayer films be used for the preparation of good quality DHI-melanin films; 2) is DHI-melanin a suitable material for supercapacitors.

These topics will be discussed from the chapter 2 onward. First, I will give a brief introduction to the materials of interest: PEDOT and melanin, and to the oxidative multilayer films.

1.1 PEDOT

The conducting polymer PEDOT (**Scheme 1**) is one of the most studied materials in the world.[32,33] It is commercially available either as a monomer (EDOT) or polyelectrolyte complex with poly(styrene sulfonate) counterion (PEDOT:PSS). Both of them are water-processable, even though the polymer itself is not water soluble, since PEDOT:PSS is dispersible in water and EDOT has a moderate solubility of 2.1 g/L[34].

Despite their name, conducting polymers are essentially nonconductive in their neutral state. However, they can be chemically or electrochemically reduced (n-doping) or, more commonly, oxidized (p-doping) to a more conductive form. The high stability of the p-doped state sets PEDOT apart from other conducting polymers.[35–39] In fact, pristine PEDOT is in a heavily oxidized state with typical 33 % oxidation level, i.e. one charge per three monomer units.[28,40] This oxidized polymer is no longer an insulator. Instead, positively charged quasiparticles (holes) can now move in the conjugated polymer matrix. PEDOT chains with odd or even oxidation levels are called a polaronic or bipolaronic state, respectively.[41] As recently reviewed by Chen et al.,[37] the conductivity of PEDOT varies highly from ~0 up to 8797 S/cm[42] and depends, e.g., on the structure and counterions in the material.

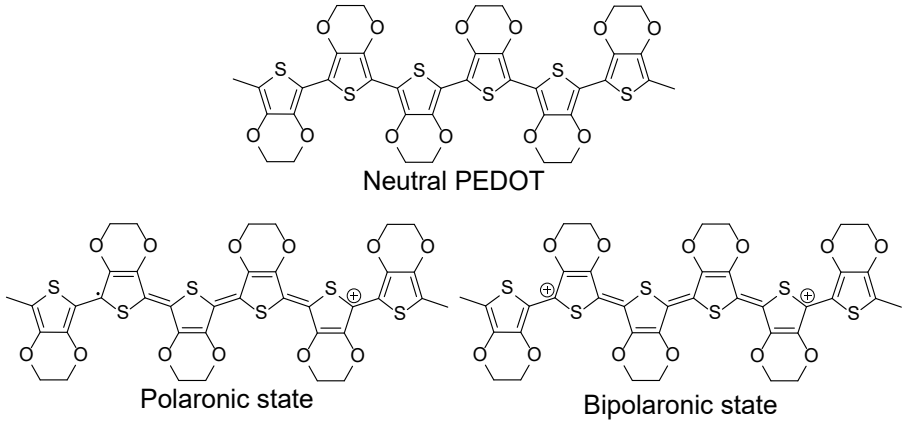

Scheme 1. Neutral PEDOT polymer chain and its polaronic and bipolaronic states. Adapted from [43].

PEDOT films can be utilized as pseudocapacitive components in supercapacitors.[44] In general, supercapacitors have long cycle life and high power density but low energy density, making them exact opposites to batteries. However, supercapacitors can be further divided into two sub-classes: electrochemical double-layer capacitors (EDLCs) and pseudocapacitors. The former store energy electrostatically within the electrical double layer at the electrode–solution interface.[**article II**] Pseudocapacitors, on the other hand, store the energy in the oxidation state of the electroactive materials in addition to the interfacial electrostatic double layer.[**article II**] The pseudocapacitive behavior brings the materials closer to batteries: improving their energy density while decreasing their power density and cycle life.

PEDOT is among the three main conducting polymers studied as a supercapacitor electrode materials together with polyaniline and polypyrrole.[45] Based on density functional theory (DFT), theoretical volumetric capacitance of

PEDOT is ≈100 F/cm^3.[46] Its mass capacitance is ca. 100 F/g[47,48] and ca. 30 F/cm^3[49,50] or 330 F/cm^3[51] volumetric capacitances have been reported for PEDOT-based materials. However, pure conducting polymers have shown many problems for the application such as relatively poor electrical conductivity, low energy density or poor cyclic stability.[45] Scientists are actively trying to overcome these challenges by composite fabrication, and many recent reviews highlight the potential to achieve further technological advances in the area, e.g., by mixing conducting polymers with metal oxides and/or carbon materials.[44,52,53] Much work has been done in the field already, but it is a major challenge to optimize the favorable interfacial connections in these multiphase materials.[27,44,52] According to the detailed review of PEDOT-based composites as the active materials of supercapacitors by Zhao et al.,[44] the mass capacitances of PEDOT/Carbon and PEDOT/MnO_2 nanocomposites are in the order of ~200 F/g, but much higher values have been reported as well. In the Chapter 1.3, I introduce still relatively little explored template polymerization method for the conducting polymer/graphene oxide composite film fabrication: oxidative multilayer films [**articles II, III**].

1.2 Melanin

Melanins have been a hot topic in materials research since the article by Lee et al. in 2007.[54] They reported that various substrates can be easily coated with mussel-inspired synthetic eumelanin analog polydopamine simply by immersing the objects in a dilute aqueous solution of dopamine. At its simplest, the process is initiated by the oxidation of dopamine by dissolved oxygen (autoxidation)[54,55] that accelerates with increasing pH [**article I**]. In their review, Ryu, Messersmith and Lee state[55] that the range of surfaces that have been successfully coated with polydopamine is nowadays very broad and includes materials with low surface energy like graphene[56] that are normally very difficult to coat. As a consequence, polydopamine coating has been called as the first material-independent surface chemistry process that modifies the properties of virtually any surfaces.[57] In addition to the simplicity and versability of the method, it is very cost effective (solid dopamine·HCl from Sigma-Aldrich costs less than 5 € per gram[58]).[55] Finally, polydopamine contains both nucleophilic and electrophilic groups (see **Scheme 2** and the structural discussion below) and its rich chemistry allows further chemical modification of the coating[30,59] via Michael addition of amines or thiols[30,54,60], metal-ion coordination[61–63] or carbonization[64,65], just to name a few methods (see ref. [30] for an extensive review of the reaction behavior of polydopamine).

1.2.1 Family of eumelanin-like materials

There are many eumelanin-like materials besides polydopamine. First of all, eumelanins are abundant in nature and can be found, e.g., in the skin, hair and eyes of animals, and have a central role e.g., as pigments and photoprotectors.[66,67] Notably, eumelanin extracted from the cuttlefish *Sepia officinalis* is commercially available. On the other hand, synthetic eumelanin analogs can be fabricated from various precursors in addition to dopamine. Eumelanin biosynthesis begins with the oxidation of tyrosine to L-DOPA.[68,69] Other notable synthetic eumelanin precursor monomers include 5,6-dihydroxyindole (DHI), 5,6-dihydroxyindole-2-carboxylic acid (DHICA), tyramine, epinephrine, and norepinephrine.[68] Now, it is important to emphasize that even though all the above-mentioned materials are classified as natural or synthetic eumelanins, they are expected to have structural differences which induce different properties[30,68].

In addition to the choice of a precursor, the structure and properties of synthetic eumelanins depend on the reaction conditions (e.g. oxidant, pH, reaction time) and post-treatment procedures (e.g. precipitation, centrifugation, lyophilization and storage conditions).[70] In particular, the composition of eumelanin films are expected to differ from that of eumelanin particles in suspensions.[30,71] The structural variation is no doubt a huge analytical challenge and it may be misleading to compare materials prepared under different conditions[30,70] but, on the positive side, it gives a large freedom for materials design[72].

For completeness, while I focus only on eumelanin and its synthetic analogs in this thesis, I find it necessary to note that four other natural melanin classes have been found[66,73]. Sulphur containing pheomelanin and neuromelanin are found in the animal kingdom, whereas nitrogen-free allomelanin and pyomelanin are found in plants and microorganisms.[66,73]

1.2.2 Structural overview of polydopamine

The exact elucidation of the chemical composition and structure of natural and synthetic eumelanins may be impossible[30] due to their notorious structural complexity[30,72,74] and insolubility that makes them difficult to study[67]. Due to the complexity of the topic, I will only briefly summarize the excellent structural overview of polydopamine given by Liebscher,[30] adding details when relevant. (Beyond this thesis, the article by Liebscher[30] and citations within, the reader is referred to the articles by d'Ischia et al.[72], Alfieri et al.[71], Xie et al.[73], Lyu et al.[75] and citations within for more comprehensive picture.)

The simplified structure and formation of polydopamine is best outlined by the reaction mechanism that is very similar to the historical Raper-Mason scheme for the enzymatic oxidation of tyrosine to eumelanin by tyrosinase[76–78] (**Scheme 2**). In

the initial step, dopamine (DA) oxidizes to dopaminesemiquinone (DSQ), which further reacts to dopaminequinone (DQ).[**article I**] This is followed by intramolecular cyclization to leucodopaminechrome (DAL), subsequent oxidation to dopaminechrome (DAC) and molecular rearrangement to 5,6-dihydroxyindole (DHI). The final product, polydopamine, is then formed in subsequent oxidation and coupling reactions. Quinone moieties in the polydopamine are redox active and have three possible oxidation states (hydroquinone, semiquinone and quinone), leading to redox disorder.[30,79][**article I**] Further, it has been shown experimentally that polydopamine contains pyrrolecarboxylic acid units that can be explained by the oxidative degradation of indole quinone moieties (**Scheme 3**).[30,31,80] For example, in the autoxidation of dopamine, oxygen is first reduced to superoxide radical $O_2^{\cdot -}$ (or perhydroxyl radical, $HO_2^{\cdot}$ depending on the pH) and then to hydrogen peroxide in two one-electron steps.[**article I**] These highly reactive oxygen radicals can attack the material, leading to the oxidative degradation structures.[**article I**]

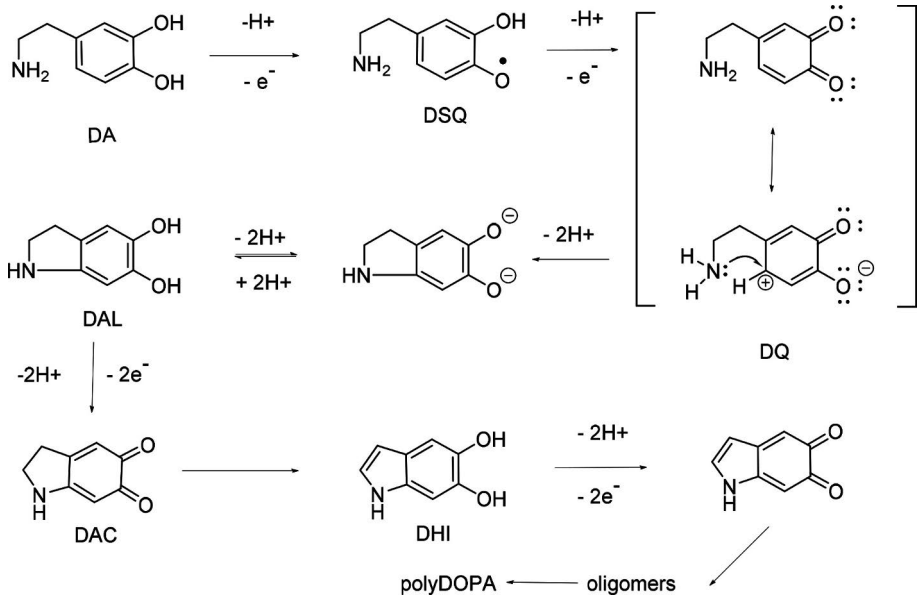

Scheme 2. Simplified reaction pathway for the oxidation of dopamine (DA) to polydopamine.[**article I**]

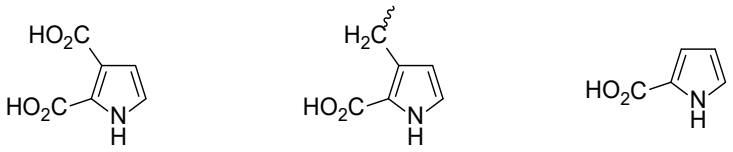

Scheme 3. Pyrrolecarboxylate units in polydopamine that form in the oxidative degradation of the indole quinone moieties. Adapted from [30].

The final product, polydopamine, can be thought as a mixture of monomers and/or oligomers with different chain lengths that form a supramolecular structure by weak interactions such as hydrogen bonding, π–π interactions, cation–π interactions and quinhydrone-like interaction.[30,31,74,80–87] However, Delparastan et al. have recently confirmed the existence of high-molecular-weight polymer chains in the polydopamine films.[74] Furthermore, while the **Scheme 2** is a well-established description of the initial steps in the dopamine autoxidation,[**article I**] its actual structure is much more complicated due to the rich reactivity of the monomer units.[30,59,71,75] For example, the oxidation pathway of dopamine is complicated by the Schiff base formation reaction between a quinone ring and an amine group, which may lead to the formation of more complicated structures (**Scheme 4**).[75] Overall, the composition of polydopamine can be significantly different to that of DHI-melanin, an eumelanin analog that is prepared by using 5,6-dihydroxyindole as a precursor.[30,71,88] However, as noted above, the reaction route can be controlled by altering the preparation conditions like dopamine concentration or oxidizing agent.[30,31,74,80] For example, low dopamine concentration increases the probability of intramolecular cyclization and can thus lead to materials resembling DHI-polymers.[31]

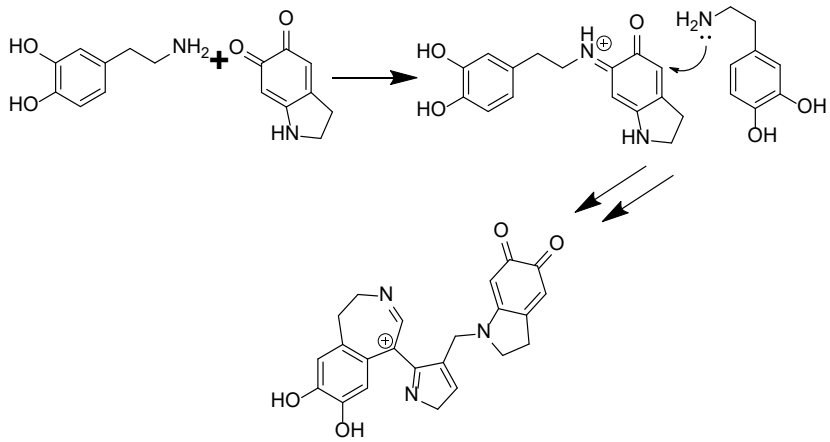

Scheme 4. Schiff base reaction between dopamine and dopaminechrome and the further product with dopaminechrome, pyrrole and benzazepine moieties that has been proposed to form in the subsequent reactions after the Schiff base formation. Adapted from [75].

To conclude, the application-oriented studies of polydopamine have expanded to nearly all areas of material science.[57] However, the studies discussing the underlying chemistry of polydopamine are still lacking,[57] which is rather surprising since, as discussed above, the structure and properties of synthetic eumelanins depend on their

preparation conditions. One particular question was highlighted in the landmark review article by Liu et al. (2014): it has not been investigated in detail why polydopamine deposition can occur under acidic conditions with the assistance of some specific oxidants.[89] In the **article I**, we present a widely applicable thermodynamic model, which clarifies the pH dependence of the critical first steps in the Raper-Mason dopamine oxidation pathway (**Scheme 2**) in the presence of dissolved oxygen and/or transition metal ions (Ce(IV), Fe(III) or Cu(II)).

1.2.3 DHI-melanin

The fabrication of DHI-melanin coatings is less straightforward since DHI is extremely air sensitive.[90–92] On the other hand, the oxidation of DHI leads to the much simpler structure compared with polydopamine, and it is mainly composed of indole-based oligomers and their oxidative degradation structures[31,71,88,93–95].

I am not aware of a thorough investigation of an effect of pH on the deposition of DHI-melanin films but it is known that, in contrary to dopamine,[54] the oxidative polymerization of DHI in alkaline pH (e.g. at pH 8.5) does not yield significant films[71,88,92]. Instead, the DHI-melanin coating deposition requires neutral or acidic pH[88,92] but the deposition kinetics have been shown to slow down when pH is decreased from 7 to 5[92]. However, even at pH 7, the self-limiting thickness of the DHI-based coating is only ca. 20 nm, much less than that of polydopamine coating prepared in the typical conditions (ca. 40 nm, 10 mM DA, Tris buffer with pH 8.5).[92] The results by Lyu et al. suggest that monomeric DHI-species, low-molecular-weight oligomers and/or small aggregates can adhere to the surfaces but large aggregates no longer cannot.[92] Competing and unavoidable aggregation of DHI in the solution phase can thus lead to small self-limited thickness of the DHI-melanin coating.[92] In another study, Arzillo et al. have shown that the hydrodynamic radius of DHI-melanin aggregates can grow up to value of ~1200 nm before precipitation and DHI polymers grow principally via monomer-polymer or small oligomer-polymer coupling instead of large oligomer-oligomer interactions.[95]

Eumelanins are partially soluble in alkaline aqueous solutions like ammonia and can be simply spin coated onto hydrophilic substrates after ultrasonication and centrifugation.[96,97] The downside is that high pH can damage the material by causing aromatic ring fission.[97,98] This and other above-described challenges in the DHI-melanin coating highlight the importance to study more advanced DHI-melanin film fabrication methods. DHI-melanin has received much less attention compared with polydopamine but various advanced film fabrication procedures like matrix assisted pulsed laser evaporation,[99] electrochemical polymerization[90,100] and ammonia-induced solid state polymerization[101] have been reported in the literature. Our group has previously shown that DHI can be oxidized onto thin oxidative

films[102] and in this thesis work, successful fabrication and electroactivity of such films was demonstrated using the developed, about ten times thicker graphene oxide (GO) containing oxidative multilayer films [**article III]** (see Chapter 1.3).

1.2.4 Electrochemical properties of eumelanin

Before moving to the fabrication of oxidative layer-by-layer films, I will briefly introduce the fascinating electrochemical properties of eumelanin materials. Eumelanin is a hybrid electronic-ionic conductor, and its conductivity depends highly on its hydration level.[103–105] Electrical properties of hydrated eumelanin films can be described with an interplay between proton migration, electronic transport, and redox processes.[104] First of all, eumelanin is redox active and hydroquinones (H_2Q) can undergo two one-electron oxidations to first to the semiquinone (SQ) form and further to the quinone form (Q). The equilibrium concentrations of these redox states is defined by the comproportionation equilibrium (**Scheme 5**).[105] It is evident from the Le Châtelier's principle that the semiquinone concentration increases with pH but hydration perturbs the comproportionation equilibrium in a similar fashion, increasing the semiquinone free radical and proton concentrations.[105] Protons can migrate in the material under the external electric field, resulting in ionic conductivity, while electrons can move within the conjugated aromatic matrix or via comproportionation equilibrium and various redox reactions.

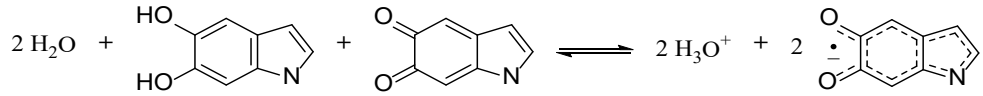

Scheme 5. Eumelanin comproportionation equilibrium (adapted from [106]).

The electronic conductivity of eumelanin has recently received more attention as Migliaccio et al. reported an unprecedented 318 S/cm conductivity for the mainly electronically conductive DHI-melanin film that had been thermally annealed in vacuum.[103] In comparison, Wünsche et al. obtained mainly ionic (largely protonic) ~10^{-3}–10^{-4} S/cm conductivity for the commercial eumelanin (synthesized by oxidation of tyrosine) at 90% relative humidity.[104] The vacuum annealing of the DHI-melanin film increased its conductivity up to over 9 orders of magnitude and this was attributed to the structural reorganization of the material which increased both the delocalization of the aromatic systems and their π-stacking interactions.[103] Carboxylic groups and bound water were evicted from the material during the annealing and the conductivity of the film actually decreased if it was exposed to water.[103] Finally, eumelanin composites have been fabricated by mixing it with more conductive materials,[107–110] representing another potential approach for the device-

quality material fabrication. In particular, material hybridization can also enhance packing of eumelanin, decreasing the spacing between elementary units and π-π stacking distance.[107]

As stated above, optimization of the interfacial connections of hybrid materials is critical in the development of supercapacitor electrode materials.[27,44,52] This was clearly seen in the recent research by Santato and others.[24,27] In the earlier study,[24] they prepared a melanin-based supercapacitor electrode with 5.6 mF/cm^2 (167 F/g) capacitance at 5 mV/s sweep rate by drop-casting commercial eumelanin on carbon paper. However, the electrode had poor rate response which, together with the relatively low capacitance, was attributed to the low electronic conductivity of eumelanin and high contact resistance between eumelanin and carbon current collector.[24,27] However, in their later study, they obtained significantly better capacitance (1355 mF/cm^2 or 452 F/g) and rate response values by chemically engineering the eumelanin/carbon paper interface prior to *Sepia* melanin deposition on the treated carbon paper.[27]

1.3 Oxidative multilayer films

Oxidative multilayer films are a general technology platform for the electrodeless oxidative polymerization of various monomers to functional films.[102,111–113][**articles II, III]**

Oxidative films can be fabricated on a wide variety of substrate materials with various layer-by-layer (LbL) self-assembly techniques. The simplest way is the dip-LbL method: the chosen charged substrate is immersed alternatively in the polycation and polyanion solutions, separated by washing steps. A good example of a LbL film is $(PSS/PAH)_n$; a multilayer film of the sodium salt of poly(styrene sulfonate) and poly(allylamine hydrochloride), where the electrostatic attraction between oppositely charged macromolecules acts as a driving force for multilayer buildup.[114] Oxidative multilayer films, on the other hand, are based on reversible coordinative bonding between a redox-active transition metal ion, e.g., Ce(IV), and a binder(s), e.g., polyphosphate (PP) and graphene oxide (GO).[102,111–113][**articles II, III]**

Freshly prepared oxidative multilayers are simply immersed in the desired monomer solution, e.g., pyrrole, EDOT or DHI, and the monomer polymerizes onto the oxidative film.[102,111–113][**articles II, III]** The amount of oxidant is the limiting factor in the process and its quantity can be controlled by adjusting the film thickness, i.e., the number of layers in the film. Our research group has focused on the study of cerium(IV) containing oxidative films that have high oxidation potential at acidic pH,[112][**article I**] but by using thermodynamic calculations, we have shown

that redox active biometals iron(III) and copper(II) are promising active ions for the oxidative multilayers as well[**article I**].

Simple dip-LbL polyphosphate/Ce(IV) multilayer films are already suitable for the surface-controlled oxidation[102,111,112] but the addition of graphene oxide as a third component in the films enhances the film growth and their mechanical properties[113]. GO is inexpensive and its water suspension can be readily used as a precursor of oxidative multilayers after ultrasonication (to exfoliate the GO sheets) due to its anionic charge and coordinative properties.[113][**article II**]

1.3.1 Oxidative spin-spray-$(PP/Ce/GO/Ce)_n$ multilayers

The simple, facile, and versatile dip-LbL film fabrication method is not without its weaknesses. Deposition of the individual layers and the subsequent rinsing of the film is often slow (e.g. >20 min for the GO containing oxidative multilayers[113]) and the material consumption in the method is high. In addition, Ce(IV)-based dip-LbL oxidative films grow exponentially with the number of deposited layers[111,113] due to vertical diffusion[115] of cerium ions in and out of the film during its assembly (internal diffusion of PP chains is also probable in the GO containing films)[111,113]. As a result, the morphology of the dip-LbL $(GO/Ce/PP/Ce)_n$ is not well-defined, GO sheets in the films are randomly oriented, the surface roughness of the films is very high and the film thickness cannot be controlled with a nanometer-level precision.[113][**article II**]

In order to improve the film properties, we studied the fabrication of $(PP/Ce/GO/Ce)_n$ multilayers with a more advanced, automated spin-spray LbL film assembly technique.[**articles II, III**] The spin-spray LbL method combines many advantages of the spin-LbL and spray-LbL methods[116–120][**articles II, III**] and its potential in the fabrication of battery electrodes has been demonstrated in the literature[117,121].

First of all, the spray-LbL method, introduced in 2000 by Schlenoff et al.,[122] is suitable for a much faster fabrication of homogenous and smooth films compared with the dip-LbL method[123]. At its simplest, reagents can be sprayed on a vertically oriented substrate using e.g. common air pump spray cans.[123] The substrate can be slowly rotated (e.g. 10 RPM) to avoid drip patterns and the method can be scaled up for industrial applications.[124]

Another popular method, spin-LbL, is likewise suitable for the rapid fabrication of multilayer films with highly ordered internal structure and low surface roughness.[125] Typically, the reagents are sequentially dropped onto a rapidly spinning substrate (e.g. 4000 RPM) or alternatively onto a stationary substrate that is then spun. In the method, the reagent adsorption and the structural rearrangement of the film happen simultaneously as centrifugal, air shear, and viscous forces cause

desorption of weakly bound material from the film.[125,126] Overall, as reviewed by Richardson et al.,[126] both spin-LbL and spray-LbL methods generally lead to stratified multilayer structure while layers of the dip-LbL films are typically interpenetrated.

The spin-spray LbL film assembly can be easily automated and the preparation of the oxidative $(PP/Ce/GO/Ce)_n$ multilayer films with the method is illustrated in the **Scheme 6**. Briefly, the substrate is attached on a horizontally oriented spinner and spun constantly during the entire multilayer film assembly process. The automated spraying unit sprays a small volume of the first reagent for t_1 seconds, followed by drying for t_2 seconds. Next, the film is rinsed with water for t_3 seconds, followed by drying for t_4 seconds. The film assembly is continued until the desired number of layers have been deposited. The individual layers are thinner than those prepared with the dip-LbL method and the deposition of an individual (PP/Ce/GO/Ce) tetralayer with the $t_1 = 3$ s, $t_3 = 10$ s, $t_2 = t_4 = 20$ s sequence takes less than four minutes.[113][**article II**] The buildup procedure can be further accelerated if desired.[117] Additionally, multiple parameters like reagent concentration, the addition of salt to the reagent solutions, substrate spin rate, reagent and rinsing solution volume and temperature are adjustable, allowing nanolevel control over the multilayer deposition.[116–118] Notably, the film fabrication with very small reagent quantities is possible, thereby greatly reducing material waste.[116,117]

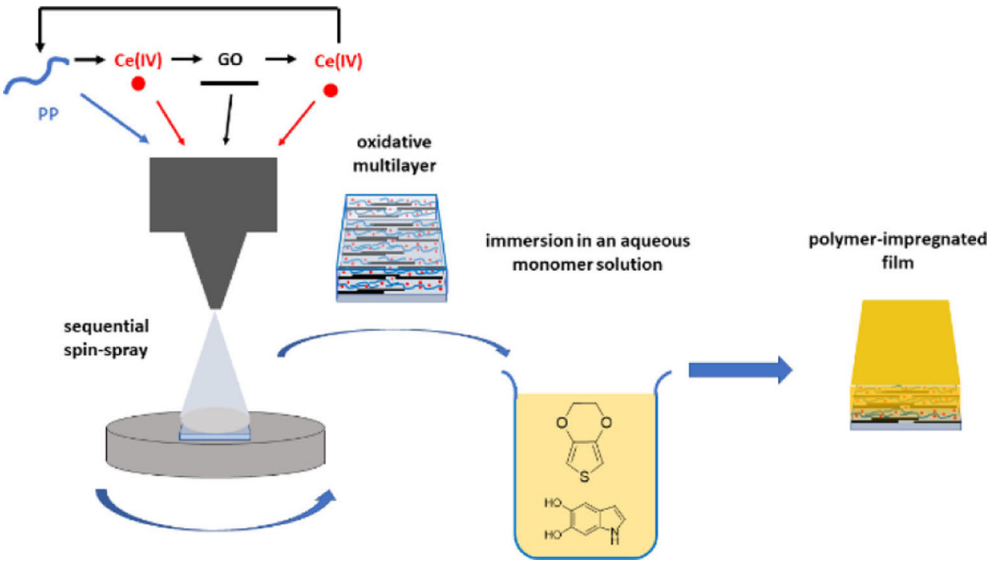

Scheme 6. Preparation of the oxidative multilayer using the automated spin-spray layer-by-layer technique and the polymerization of chosen monomer (EDOT or DHI in the figure) onto the oxidative film.[**article II**]

1.3.2 Comparison of oxidative multilayers to other techniques

The oxidative multilayer films can be conveniently compared with the other oxidative polymerization techniques by using the PEDOT film deposition from the EDOT monomer as an example. An excellent overview of the oxidative chemical polymerization of EDOT can be found in the recent review by Gueye et al.[36] and will be briefly summarized here, adding details when relevant.

First of all, PEDOT can be polymerized simply by adding oxidants in its monomer solution, but the product is insoluble and infusible and therefore difficult to process.[36,127] In 1990, however, Bayer AG introduced a landmark synthesis method of PEDOT.[36] EDOT is polymerized in an aqueous solution with PSS polyanion using $Na_2S_2O_8$ as an oxidant. In this case, PSS counter-anions stabilize the polymer and the processable dispersion of PEDOT:PSS is formed. The conductivity of PEDOT:PSS films can be significantly enhanced by a simple chemical treatment: the immersion of the PEDOT:PSS thin film to the H_2SO_4 solution decreases the PSS content in the material and 100 % sulfuric acid increased the conductivity of the film from 787.99 to 4839.92 S/cm.[128]

In vapor phase polymerization (VPP), as performed by Winther-Jensen et al., an oxidant, Fe(III)tosylate in butanol, is first mixed with an alkaline inhibitor pyridine to prevent an acid-initiated polymerization of EDOT at very acidic pH (the addition of pyridine raises the pH of the mixture to roughly 2.5).[129,130] The mixture is distributed on a substrate, dried, and moved to the VPP chamber that contains an EDOT reservoir and is filled with EDOT vapor.[129] The chamber is flushed with N_2. The pyridine inhibitor slowly evaporates in the chamber and the polymerization of EDOT starts. The substrate is kept inside the chamber for 1 h and a film with very high (>1000 S/cm) conductivity is obtained.

Oxidative chemical vapor deposition (oCVD) is a solventless method where EDOT and $Fe(III)Cl_3$ vapors are introduced to a temperature-controlled substrate in a vacuum chamber.[131] The thus obtained PEDOT film is then rinsed with HBr and methanol to remove the residual oxidant and unreacted monomers and films with very high >1000 S/cm conductivity are again obtained.

Contrary to the highly specialized oxidative vapor deposition techniques, the liquid phase depositional polymerization (LPDP) method[132–135] uses a much simpler approach. Essentially, a pre-treated substrate coated with an oxidant, e.g. Fe(III) p-toluenesulfonate with pyridine additive, is immersed in the EDOT solution in a solvent in which the oxidant is practically insoluble, e.g. n-heptane.[134] Films with relatively high conductivity (up to 530 S/cm) have been obtained with the method.[133–135] The LPDP method closely resembles the use of oxidative films to the chemical oxidative polymerization. However, the multilayer approach enables one to control the amount of oxidant on the substrate by simply adjusting the number of

layers in the oxidative film.[**article II**] In addition, the preparation of oxidative multilayers and the post-assembly polymerization can be done using only aqueous solutions (apart from the substrate pre-treatment) and hazardous organic solvents like n-heptane are not needed.

2 Results and Discussion

In this chapter, I will summarize the results in the **articles I–III**. The reader is referred to the original publications and references within for experimental sections, derivation of all the equations and other additional information.

2.1 The oxidation of dopamine to polydopamine

As described above, the mussel-inspired polydopamine coating is a simple, cost-effective, and versatile method to modify the properties of virtually any surface.[54,55,57] Simple dissolution of dopamine to mildly alkaline aqueous buffer solution results in the polydopamine formation in solution and on various surfaces. Our aim was to clarify the pH-dependence of the oxidation of dopamine both in autoxidation and in the presence of transition-metal ions. We used a thermodynamic analysis of the process together with experimental results. The general models presented in the work are applicable to other catecholamines as well.

Due to the complexity of the dopamine oxidation process, we concentrated only on the critical initial steps of the Raper-Mason dopamine oxidation pathway (**Scheme 2**)

- The oxidation of dopamine to dopaminesemiquinone and its further reaction to dopaminequinone. These steps are practically reversible.
- The intramolecular cyclization of dopaminequinone to leucodopaminechrome. This step is practically irreversible and can drive the overall reaction forward even in the unfavorable conditions.

Secondly, we focused only on the early stages of the oxidation process and therefore complications due to the further reactions of the formed products can be neglected. Finally, we used low 0.1 mM dopamine concentration. Low dopamine concentration (e.g. 0.5 mM) increases the probability of intramolecular cyclization to eventually create DHI, while dopaminequinones in high dopamine concentration (e.g. 10 mM) are more susceptible to other competing pathways such as dimerization.[31] Polydopamine from a low 0.5 mM dopamine precursor already resembles the DHI-polymers.[31]

2.1.1 Effect of pH on the first steps of dopamine autoxidation

I begin by considering the oxidation of dopamine to dopaminesemiquinone and its further reaction to dopaminequinone. The $O_2/O_2^{\bullet-}/H_2O_2$ redox system has a crucial role in the initial phase of the autoxidation process. The specialization of all relevant species depend on pH and their formal standard redox potentials are shown in the **Figure 1**.

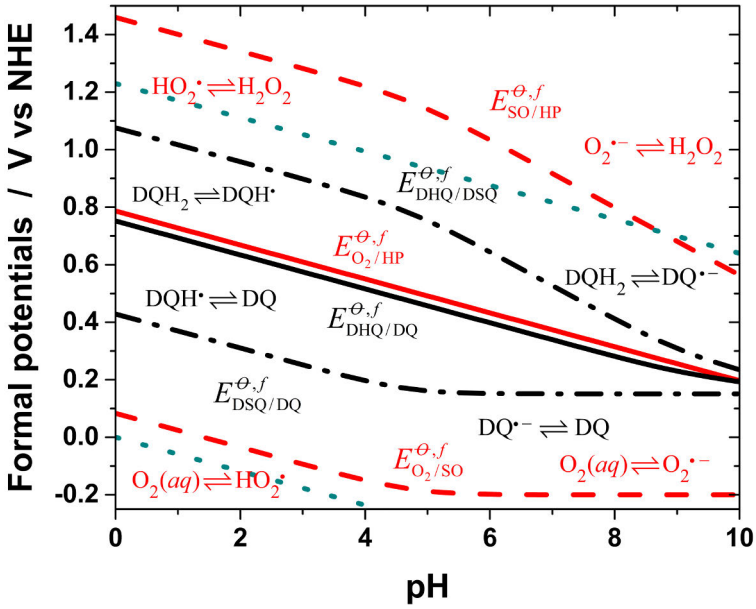

Figure 1. Formal standard two-electron (solid lines) and one-electron (dashed lines) redox potentials for the dopamine/dopaminesemiquinone/dopaminequinone (black lines) and oxygen/superoxide/hydrogen peroxide (red lines) redox systems as a function of pH. The dominant species involved at the different pH ranges are shown in the figure. Dashed dark cyan lines represent the stability range for water. All data refer to 25 °C.[**article I**, modified image]

The formal two-electron redox potentials of the $O_2(aq)/H_2O_2$ and dopaminequinone/dopamine redox pairs suggest that the two-electron oxidation of dopamine by O_2 is thermodynamically favorable over the whole pH range. However, this pathway can be ruled out since oxygen has a triplet ground state ($^3\Sigma_g$) and its two-electron redox reactions with organic species, which are usually in singlet states, are spin-forbidden.[136–139] This creates a large activation barrier and makes the reactions slow. Therefore, the first reaction in the autoxidation process is the one-electron oxidation of dopamine by O_2.

$$O_2(aq) + DHQ \rightleftharpoons SO + DSQ \quad (1)$$

where acronyms DHQ, SO and DSQ are used for dopaminehydroquinone, superoxide and dopaminesemiquinone, respectively, irrespective of their protonation state. **Figure 1** shows that the reaction (1) is thermodynamically unfavorable in the entire studied pH-range, although it becomes less so at pH > 5. However, the superoxide and perhydroxyl radicals are strong oxidants and can oxidize both dopamine and dopaminesemiquinone species. The reaction (2) between the superoxide and semiquinone should be the most important pathway to proceed in the initial phase of the autoxidation process since this reaction is thermodynamically highly favorable and SO and DSQ are very close to each other after the initial reaction (1), possibly still within the encounter complex.

$$SO + DSQ \rightleftharpoons HP + DQ \quad (2)$$

where HP and DQ are used for hydrogen peroxide and dopaminequinone respectively. The significance of other reaction pathways such as dopamine oxidation by SO and semiquinone disproportionation reaction (3) increase when more SO and DSQ have been generated in the solution, but we limited the discussion of the oxidation process mainly to the initial phases of the process.

$$2DSQ \rightleftharpoons DQ + DHQ \quad (3)$$

The next critical step in the dopamine's Raper-Mason reaction pathway (**Scheme 2**) is the practically irreversible intramolecular cyclization of dopaminequinone to leucodopaminechrome. The reaction takes place as a Michael N-addition of the unprotonated amino group to the oxidized catechol ring. We describe the initial steps in dopamine autoxidation by the following simple model (DAL = leucodopaminechrome, DAC = dopaminechrome):

$$DHQ + O_2(aq) \underset{k_{1b}}{\overset{k_{1f}}{\rightleftharpoons}} DSQ + SO \underset{k_{2b}}{\overset{k_{2f}}{\rightleftharpoons}} HP + DQ \xrightarrow{k_c} DAL \underset{k_{3b}}{\overset{k_{3f}}{\rightleftharpoons}} DAC \quad (4)$$

where k_{1f}, k_{1b}, k_{2f}, and k_{2b} are the average apparent one-electron-forward- and backward-charge-transfer rate constants for the first and second redox steps, respectively, and k_c is the apparent first-order rate constant for the ring closure. Using the classical Marcus theory as an approximative model and different levels of other approximations (see **article I** and references within for details), the formation rate of DQ can be expressed as

$$\frac{d[\mathrm{DQ}]}{dt} = \frac{k_{1f}k_{2f}K_1}{(k_{1f} + k_{2f}K_1)} C_Q C_{O_2} e^{-k_c t} = \xi_{\mathrm{DQ}}(\mathrm{pH}) e^{-k_c t} \tag{5}$$

and the formation rate of leucodopaminechrome as

$$\begin{aligned} \frac{d[\mathrm{DAL}]}{dt} &= \frac{k_{1f}k_{2f}K_1}{\left(k_{1f} + k_{2f}K_1\right)} C_Q C_{O_2}[1 - e^{-k_c t}] \\ t \ll 1/k_c \\ \approx \quad & \frac{k_c k_{1f}k_{2f}K_1}{(k_{1f} + k_{2f}K_1)} C_Q C_{O_2} t = \xi_{\mathrm{DAL}}(\mathrm{pH}) t \end{aligned} \tag{6}$$

where $K_1 = \frac{k_{1f}}{k_{1b}}$. Dopamine and dissolved oxygen concentrations C_Q and C_{O_2} are assumed to remain constant during the initial stages of the reaction.

The initial DQ-formation rate (ξ_{DQ}) and the proportionality factor of the DAL-formation rate at $t \sim 0$ (ξ_{DAL}) are plotted in **Figure 2a** at different pHs. Reorganization energies for the studied reactions were not found from the literature, but as seen from **Figure 2**, its value does not markedly affect to the form of the pH profiles.

The calculations predict that the DQ-formation rate is small and constant below ca. pH 5 but increases above it. As a result, the DAL formation rate also accelerates above pH 5 but significant acceleration is observed only above ca. 8–9 pH (see the inset in **Figure 2a** with curves on a linear scale).

We compared the model with two sets of experiments (**Figure 2b)**. First, an acidic dopamine solution was titrated with NaOH and analyzed UV-Vis spectrophotometrically. The titration method is not well-defined in a thermodynamic or kinetic sense, but it is suitable for the observation of intermediate species. Initial absorbance at 300 nm in **Figure 2b** is attributed to leucodopaminechrome based on the UV-Vis absorbance of leucodopa[140,141]. Clear absorbance at this wavelength was observed from ca. pH 5 upward and changes below this pH are attributed to local pH transients. The oxidized form of leucodopaminechrome, dopaminechrome, has a wide and distinctive absorption band at ca. 480 nm and another band at 300 nm.[142] The reaction of dopaminechrome to 5,6-dihydroxyindole is slow, which leads to its accumulation in the solution.[142,143] Rapid growth at 480 nm is not observed until ca. pH 9. Further products eventually obscure the signal of the intermediates as the reaction proceeds.

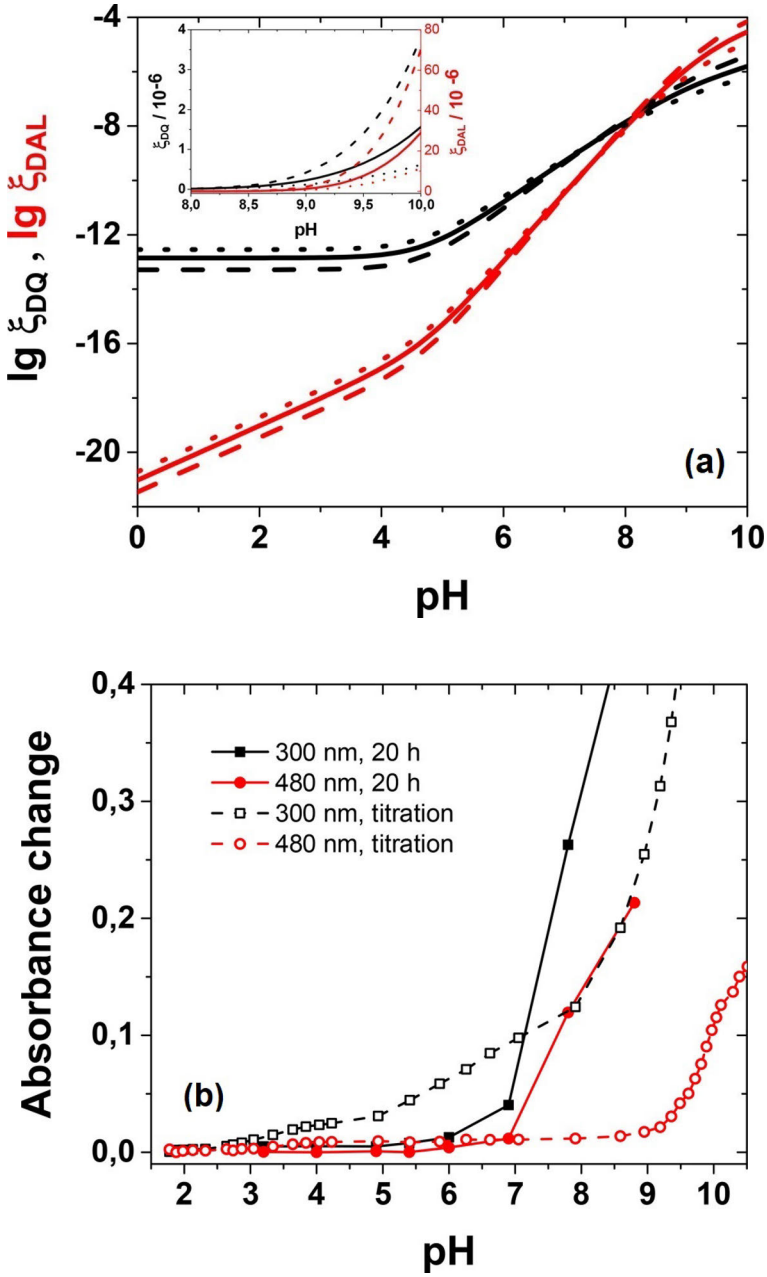

Figure 2. **(a)** Calculated pH profiles for the initial formation of dopaminequinone (ξ_{DQ}, black lines; initial rate in units of $dm^3\ mol^{-1}\ s^{-1}$) and leucodopaminechrome (ξ_{DAL}, red lines; in units of $dm^3\ mol^{-1}\ s^{-2}$, actual rate obtained by multiplying by time as long as $t \ll 1/k_c$), based on the kinetic model in the text. Calculated for $C_Q = 1\ \mathrm{mM}$, $C_{O_2} = 0.25\ \mathrm{mM}$, 25 °C and three different reorganization energies: solid lines, λ = 1.5 eV; dashed lines, λ = 1.8 eV; dotted lines, λ = 1.2 eV. The inset shows the same curves on a linear scale. **(b)** Evolution of absorbance in the autoxidation of dopamine as a fuction of pH during titration with NaOH or after 20 h of reaction time. (a),(b): [**article I**].

In our second set of experiments, dopamine solutions in a citrate phosphate buffer at different pHs were allowed to react for 20 h and the products were analyzed UV-Vis spectrophotometrically. The effective onset pH for autoxidation was again ca. 5. Overall, the experimental results are well in accordance with the calculated pH profiles for the process.

We can conclude that the decisive physicochemical parameters that control the autoxidation of dopamine are (1) the pK_a value of the hydroxyl group in the semiquinone radical (ca. 4.7[144,145]), which is the turning point of the formal potential curve of the DHQ/DSQ pair in **Figure 1**. (2) The pK_a value of the protonated amino group in the dopaminequinone (ca. 9.6[146]) since cyclization by Michael addition requires that the amino group is in an unprotonated form. At low pHs, the intramolecular cyclization of dopaminequinone is the rate-determining step in the process and the reaction slowly moves toward an equilibrium determined by the first two redox steps.

2.1.2 Transition-metal-assisted oxidation of dopamine

It is known that redox-active transition metals like Ce(IV), Fe(III) and Cu(II) can induce dopamine oxidation in weakly acidic solutions.[102,147–149] Our aim in this work was to clarify this phenomenon. In a related research, we have shown that polydopamine particles synthesized in the presence of Ce(IV) or Cu(II) ions contain only small amounts of these ions (ca. 1-2 atomic-%) but the iron content in the Fe(III) oxidized dopamine is significant (ca. 20 atomic-%).[61] Both alternatives are interesting since metal ions can improve the properties of melanins, e.g. their conductivity[106].

We studied the pH dependence of dopamine oxidation in the presence of Ce(IV), Fe(III) or Cu(II) using NaOH titration or long reaction times (**Figure 3a,b**) (NaOH titration with Ce(IV) is reported in the earlier work[102]). Similarly to the autoxidation reaction, the formation of dopaminequinone was not observed (maximum at 395 nm[142]) and the initial absorbance changes at 300 and 480 nm are attributed to the formation of leucodopaminechrome and dopaminechrome respectively. The observed pH shift in the reaction onset is large, 2–6 pH units.

In order to study the enhanced reaction rate in the presence of transition metal-ions in more detail, we followed the evolution of UV-Vis absorbance in anaerobic conditions at mildly acidic pH 4.5 (**Figure 3c**). A trace for a dopaminechrome intermediate is observed in the presence of Ce(IV) and Fe(III). With Cu(II), the reaction proceeds when Cl^- ions are added to the system, and more rapidly if also oxygen is present.

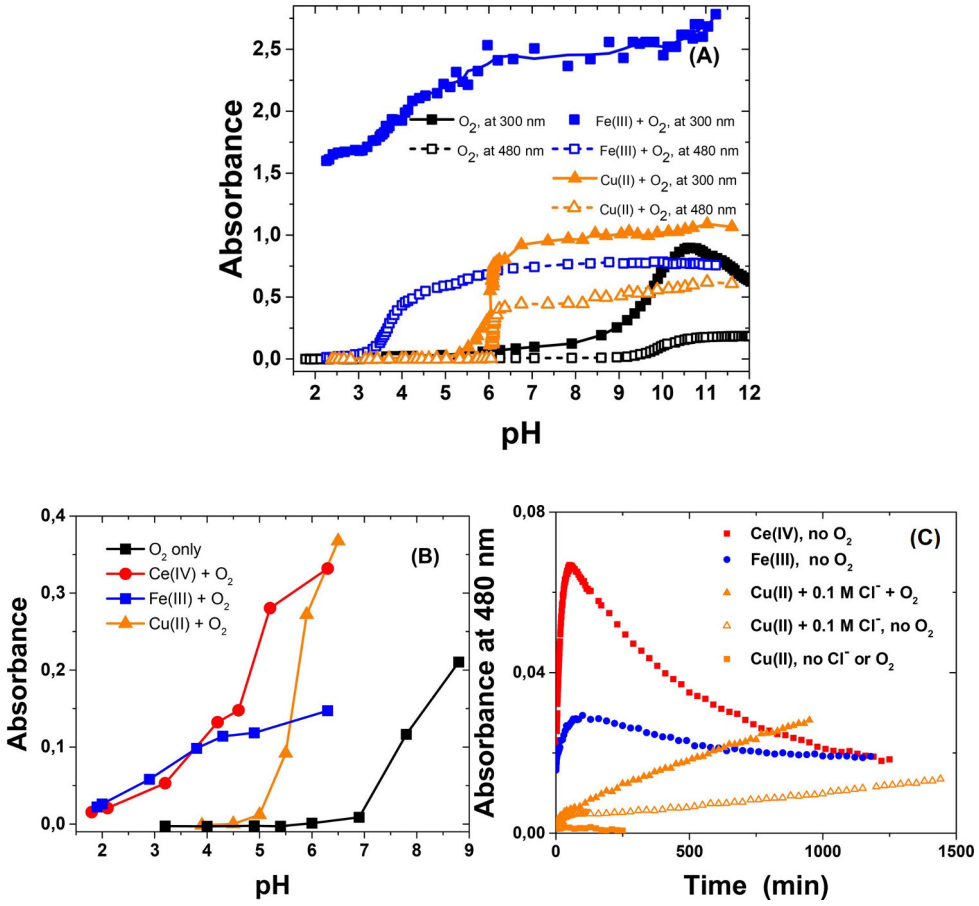

Figure 3. **(a)** Evolution of absorbance during titration of dopamine with NaOH in the presence of O_2 only or with Fe(III) or Cu(II) (10:1 metal/dopamine ratio). **(b)** Absorbance changes at 480 nm after 20 h of reaction time in the presence of O_2 only or with Ce(IV), Fe(III) or Cu(II) (4:1 metal/dopamine ratio). **(c)** Evolution of absorbance at 480 nm during the oxidation of dopamine at pH 4.5 in the presence of Ce(IV), Fe(III) (1:1 metal/dopamine ratio) or Cu(II) (6:1 metal/dopamine ratio). (a)–(c): [**article I**].

In order to justify the observations, we have constructed the Pourbaix diagrams of the metal-ions (**Figure 4a**, note that their redox properties are strongly dependent on the ambient. This is discussed in the **article I**). Dopamine is a strongly complexing ligand but assuming reversible complex formation and intracomplex charge transfer, the complexation with an innocent redox-active ligand is thermodynamically identical to the case with no metal complexation. Therefore, the presence of dopamine is not assumed to influence the oxidizing power of the studied redox-active metal ions. Notably, chloride ions enhance the oxidizing power of the Cu(II)/Cu(I) redox pair, in accordance with previous studies[144]. We attribute this effect to the stabilization of Cu(I) by soluble chloro complexes.

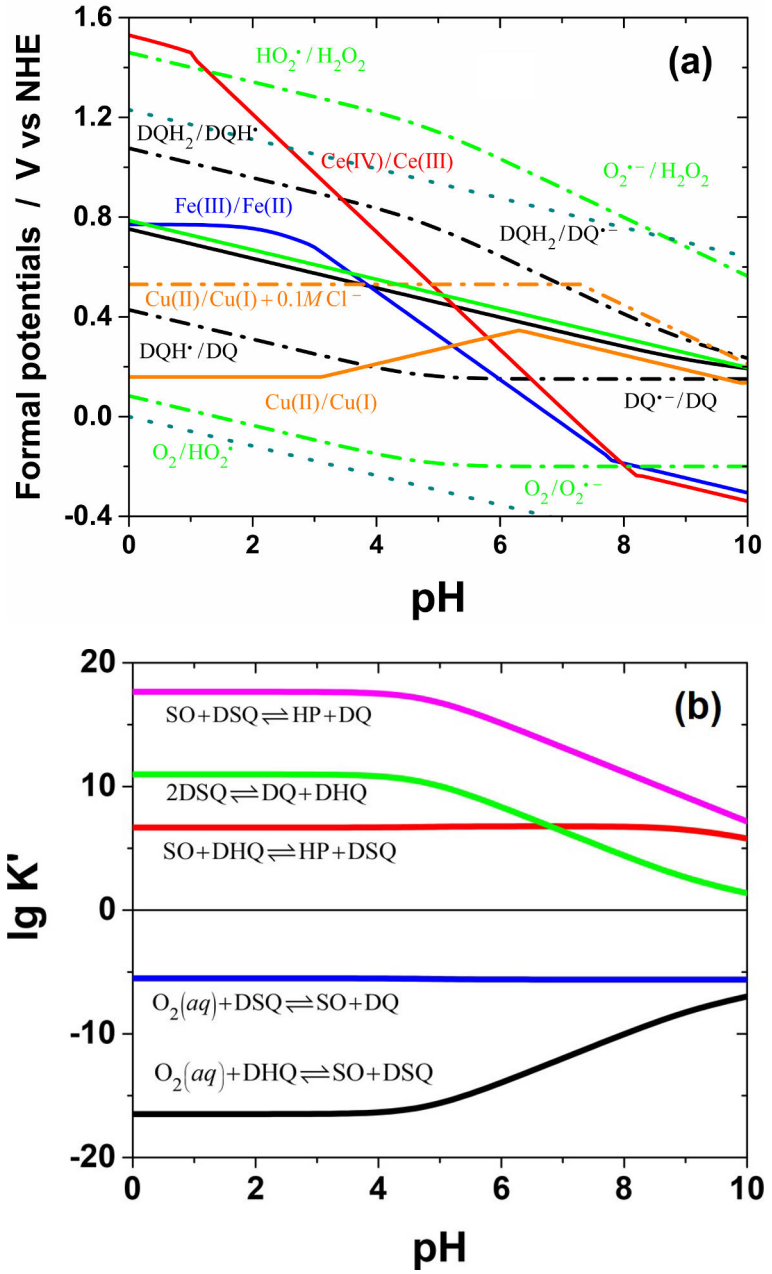

Figure 4. **(a)** Calculated formal one-electron potentials of the Ce(IV)/Ce(III), Fe(III)/Fe(II), Cu(II)/Cu(I), and Cu(II)/Cu(I)+Cl^- redox systems as a function of pH. Dopamine and oxygen redox systems are also included for comparison. The solid black and green lines are the two-electron formal potentials of the dopamine/dopaminequinone and oxygen/hydrogen peroxide pairs, respectively. Dashed dark cyan lines represent the stability range for water. See **article I** for concentrations and other experimental details. **(b)** Conditional equilibrium constants (K') as a function of pH for redox reactions between oxygen and dopamine species. (a): [**article I**, modified image]; (b): [**article I**].

Figure 4a shows that Ce(IV) and Fe(III) are highly oxidizing only in acidic conditions. Still, the oxidation of dopamine at pH 4.5 in Ce(IV), Fe(III), and Cu(II)+Cl^- solutions proceeds at a reasonable rate. In the absence of oxygen, the oxidation of dopamine to dopaminesemiquinone by the metal-ions is the first reaction in the dopamine-oxidation process. The process can continue via multiple pathways. Semiquinones can disproportionate or be oxidized by metal-ions. The presence of dissolved O_2 further accelerates the oxidation process. For instance, O_2 can oxidize dopaminesemiquinones to dopaminequinone:

$$O_2 + \mathrm{DSQ} \rightleftharpoons \mathrm{SO} + \mathrm{DQ} \qquad (7)$$

The reaction (7) has a low equilibrium constant (**Figure 4b**) but it is driven to the right since DQ quickly cyclizes and superoxide is a strong oxidant and can easily react further.

Finally, it is important to consider whether the transition metals can enhance the dopaminequinone cyclization reaction. The absorbance increase rate at 480 nm (**Figure 3c**) allows to estimate the dopaminechrome-formation rate coefficient as 2.3 x 10^{-4} s^{-1} under anaerobic conditions in the presence of Ce(IV). The kinetic modelling of the dopamine autoxidation yields a value of 2.0 × 10^{-4} s^{-1} for the dopaminequinone cyclization rate at pH 4.5. The values are in very good accordance with each other and suggest that the unassisted rate of ring closure is enough to cyclize practically all dopaminequinone formed in the Ce(IV)-enhanced oxidation. The dopamine oxidation reaction is slower in the presence of Fe(III) or Cu(II)+Cl^- at pH 4.5 compared to Ce(IV). Therefore, the thermodynamic enhancement of dopamine oxidation by metal-ions is enough to explain the accelerated dopaminechrome formation in the studied reaction conditions. At low pH, the dopaminequinone cyclization will become rate-determining.

2.2 Oxidative multilayer films

In the second part of the thesis, I will present our process of enhancing the oxidative multilayer fabrication. In addition, I will present results of the use of oxidative films for the deposition of thin redox-active and capacitive films.

- I will begin by introducing the operating principle of oxidative $(PP/Ce/GO/Ce)_n$ multilayer films and the roles of polyphosphate (PP), graphene oxide (GO) and Ce(IV)-ions in the film.
- Secondly, I will present the advantages of the spin-spray LbL method in the oxidative film fabrication over the traditional dip-LbL method.
- Thirdly, I will discuss the electrochemical properties of the spin-spray $(PP/Ce/GO/Ce)_n$/PEDOT films in detail.
- Finally, I will describe the structure of the spin-spray $(PP/Ce/GO/Ce)_n$/(DHI-melanin) films in detail, and briefly introduce their electrochemical properties.

Two experimental details should be noted. (1) All electrochemical studies were performed using a three-electrode configuration with Ag/AgCl reference electrode. (2) The composition of the films was studied primarily with X-ray photoelectron spectroscopy (XPS). It is a surface analysis technique that provides information from the top 1–10 nm of the sample. Therefore, the film interior was studied by sputtering the samples with relatively low energy argon gas cluster ion beam. This minimizes the chemical changes of polymeric materials during the sputtering.[150,151]

2.2.1 The operating principle of oxidative $(PP/Ce/GO/Ce)_n$ multilayer films

As discussed in the introduction, oxidative $(PP/Ce/GO/Ce)_n$ multilayer films are a general technique for the oxidative polymerization of various monomers to functional films.[102,111–113] Our group has previously shown that graphene oxide (GO) improves the growth and mechanical properties of the films. Ce(IV) acts as oxidant and the oxidation potential of the Ce(III)/Ce(IV) redox pair increases with decreasing pH (**Figure 4a**).[112,113] Polyphosphate (PP) binds the oxidative multilayers together. However, polyphosphate degrades hydrolytically in aqueous solutions, and in accordance with the literature,[152–154] we showed with ^{31}P NMR (nuclear magnetic resonance spectroscopy) that the process accelerates significantly with decreasing pH. Different metal cations may also either enhance or inhibit the degradation.[153,154]

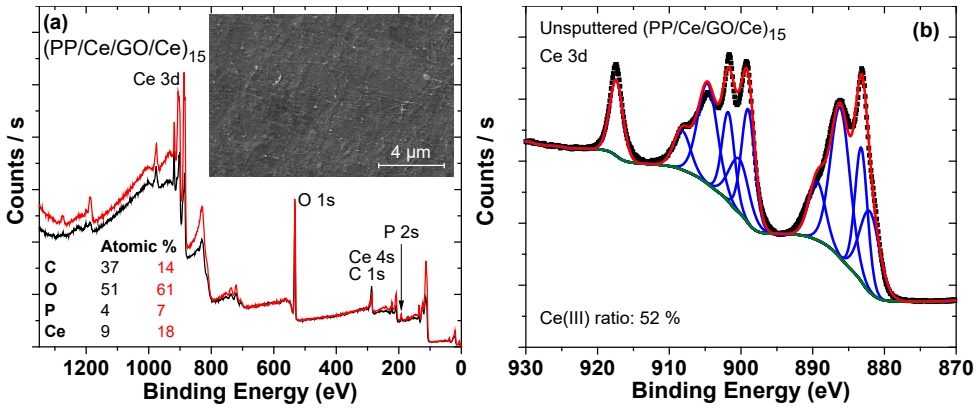

Figure 5. **(a)** XPS survey spectra of the $(PP/Ce/GO/Ce)_{15}$ film and relative atomic concentrations of surface elements before (black) and after (red) argon gas cluster sputtering for 30 s (4 eV cluster energy per atom). Inset: SEM image of the film. **(b)** Ce 3d region XPS spectrum of the unsputtered $(PP/Ce/GO/Ce)_{15}$ film and ten-peak fit to the data. Ce(III) ratio was estimated from the area of the Ce(III) peaks (see **article III** for details). (a): [**article III**]; (b): [**article III**, modified image].

X-ray photoelectron spectra (XPS) show that the oxidative $(PP/Ce/GO/Ce)_{15}$ film consists of the expected elements (C, O, P and Ce) and has Ce(III)/Ce(IV) ions in the ratio of 1:1 on its surface (**Figure 5**). Further, the relative atomic concentrations of the sputtered film in **Figure 5a** reliably represent its bulk composition since nearly the same values were also obtained with energy dispersive X-ray spectroscopy analysis (EDS). The composition of the oxidative film is discussed in detail in **article III**.

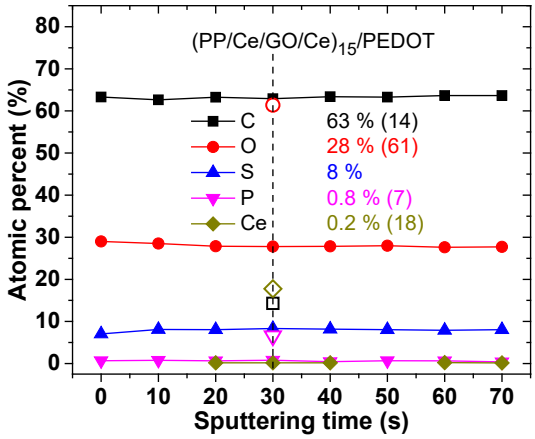

Figure 6. Depth profile of the $(PP/Ce/GO/Ce)_{15}$/PEDOT film (calculated from XPS survey spectra, argon gas cluster sputtering with 4 eV per atom). The relative atomic concentrations of the sputtered $(PP/Ce/GO/Ce)_{15}$ film are shown for comparison as open symbols and percentages in parentheses.[**article III**]

By the oxidation of EDOT onto the $(PP/Ce/GO/Ce)_{15}$ multilayer, we demonstrated that phosphates and Ce(III)/Ce(IV) ions in the oxidative film dissolve in the adjacent solution during the polymerization in highly acidic pH (pH 1.5, 17 h, **Figure 6** and **Figure 8**). The most critical step, disappearance of the Ce(IV) from the film, is almost complete e.g. in two hours with $(PP/Ce/GO/Ce)_{15}$ film (see **article II** for details). Reduced Ce(III)-ions have low complexing power, which leads to their dissolution from the film.[102] As a result, the $(PP/Ce/GO/Ce)_{15}$/PEDOT film consists of mainly of PEDOT (ca. 80 % w/w) with some graphene oxide sheets (**Figure 9**) and has very uniform depth profile (**Figure 6**).

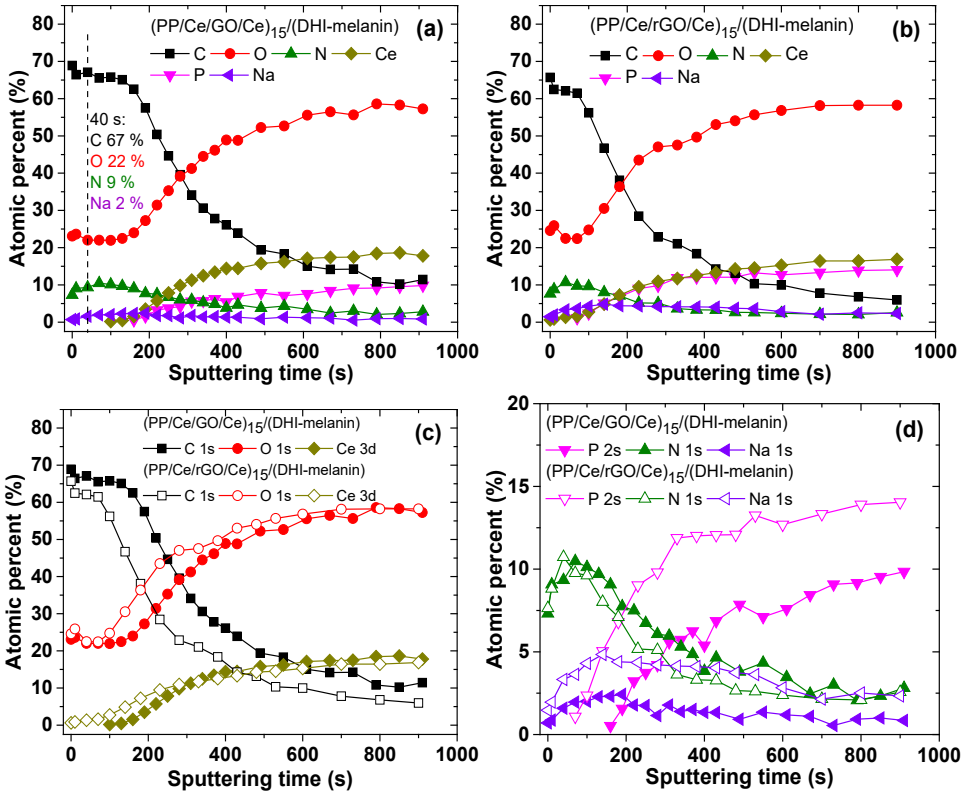

Figure 7. Depth profile of the $(PP/Ce/GO/Ce)_{15}$/(DHI-melanin) film **(a)** before and **(b)** after the electrochemical reduction of GO [calculated from XPS survey spectra (see **article III** for details), argon gas cluster sputtering with 4 eV per atom]. **(c-d)** Comparison of the depth profiles. (a)–(d): [**article III**].

On the other hand, significant PP hydrolysis did not take place during the DHI-melanin film formation onto the oxidative $(PP/Ce/GO/Ce)_{15}$ film at mildly acidic pH (2 h under ambient atmosphere, 5,6-dihydroxyindole in ethanol/water solution with pH 4.5 sodium acetate buffer). As shown in **Figure 7** and **8**,

DHI-melanin forms mainly on the outer surface of the oxidative film. The graphene oxide in the underlying oxidative multilayer can be reduced after the DHI-melanin formation, which significantly enhances the electroactivity of the films (see **Figure 15** and its discussion). Furthermore, depth profiles of the $(PP/Ce/rGO/Ce)_{15}$/(DHI-melanin) film suggest that the reduction does not have a substantial effect on the film composition (**Figure 7**).

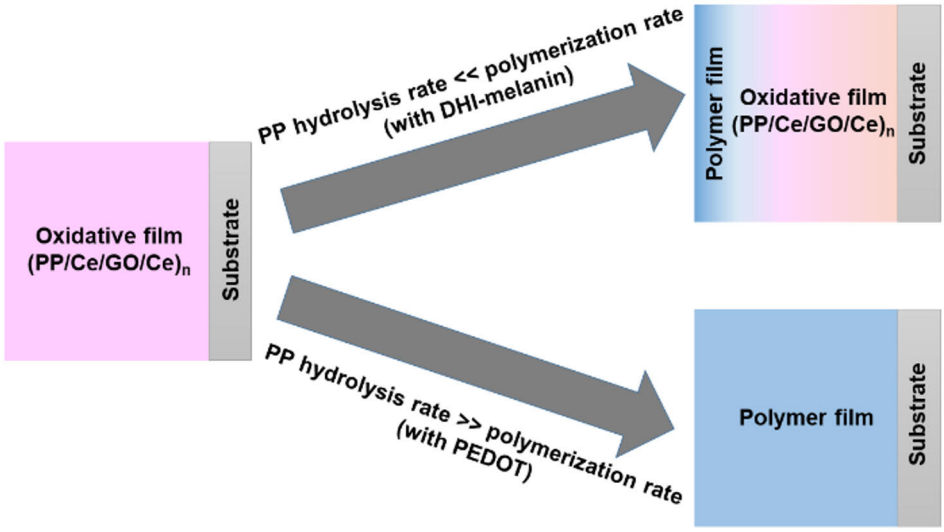

Figure 8. The role of polyphosphate hydrolysis during the polymer film formation onto the oxidative film.[**article III**]

In conclusion, polyphosphate hydrolyzes under acidic conditions and the degradation rate increases with decreasing pH. As a consequence, phosphates and cerium-ions can be dissolved from the oxidative film in the adjacent monomer solution during the oxidative polymerization. This was demonstrated by the oxidation of EDOT at pH 1.5 and the as-synthesized GO/PEDOT film has an uniform depth profile (**Figure 6**). On the other hand, DHI-melanin film formed mainly on the exterior surface of the oxidative film at lightly acidic pH 4.5, leaving the bulk of the oxidative multilayer partially intact (**Figure 7a**). In general, oxidative multilayer dissolution is expected when the PP hydrolysis rate is much faster than the polymerization rate (**Figure 8**).

2.2.2 Growth of spin-spray $(PP/Ce/GO/Ce)_n$ multilayers and advantages of the assembly method over dip-LbL

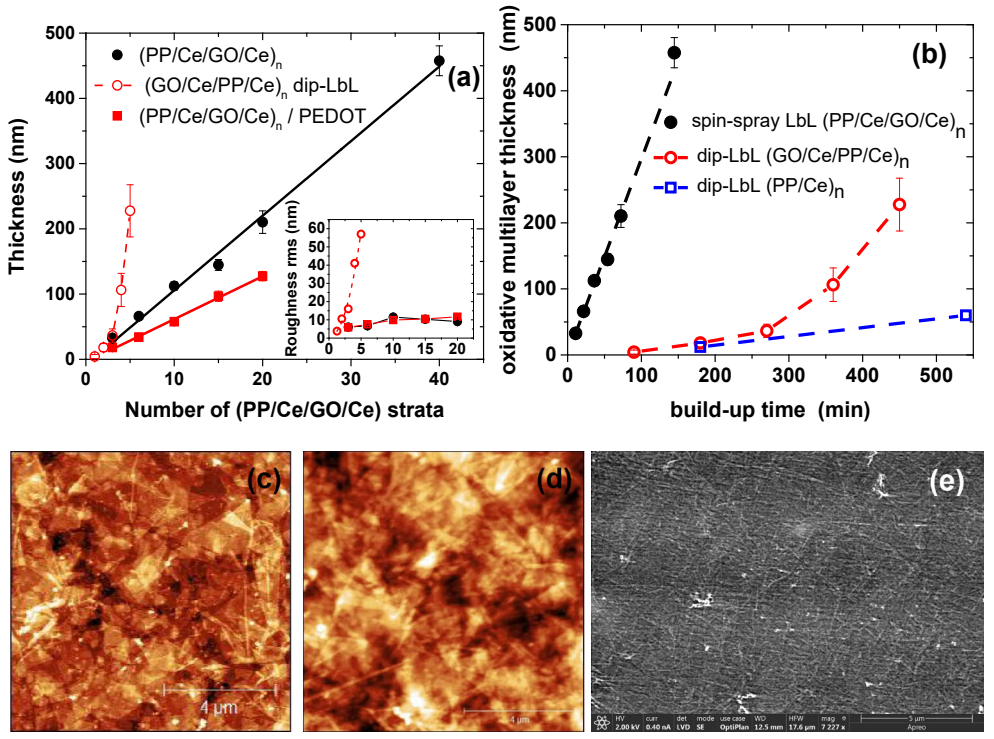

Figure 9. **(a)** Thickness of spin-spray $(PP/Ce/GO/Ce)_n$ (solid black) and $(PP/Ce/GO/Ce)_n$/PEDOT (solid red) films measured by *ex situ* AFM as a function of the number of tetralayers (n). Lines are linear fits to the data. The inset shows the rms surface roughness of the films. The behavior of dip-LbL $(GO/Ce/PP/Ce)_n$ films is shown for comparison (open red circles). **(b)** Thickness of dip $(PP/Ce)_n$, dip $(GO/Ce/PP/Ce)_n$ and spin-spray $(PP/Ce/GO/Ce)_n$ films as a function of the time required for the film build-up process. Additional details for (a) and (b) are given in **article II. (c)** 10 µm x 10 µm *ex situ* AFM images of the $(PP/Ce/GO/Ce)_3$/PEDOT and **(d)** $(PP/Ce/GO/Ce)_{15}$/PEDOT films. **(e)** SEM image of the $(PP/Ce/GO/Ce)_{15}$/PEDOT film. The data for the dip-LbL films in **Figure 9a,b** is from our earlier work.[112,113] (a),(b): [**article II**, modified image]; (c),(d): [**article II**]; (e): [**article III**, modified image].

Spin-spray $(PP/Ce/GO/Ce)_n$ films grow linearly from the beginning, by ca. 11 nm per tetralayer (**Figure 9a**), and their build-up time is much faster in comparison with the corresponding dip $(GO/Ce/PP/Ce)_n$ films[113] (**Figure 9b**). In contrast, oxidative dip-LbL films grow exponentially in the beginning (**Figure 9a**),[111,113] which is indicative of intrafilm diffusion during the assembly[111,115]. The linear growth is typical to spin-spray LbL films[116,117] and can be attributed to the high shear stress within the thin solution layer and its rapid drying, which shortens the time available for structural rearrangements or diffusion during the assembly process[118,117,120]. The

thickness of the $(PP/Ce/GO/Ce)_n$/PEDOT films is thinner than that of the original oxidative films (ca. 7 nm per (PP/Ce/GO/Ce) strata) due to the dissolution of the oxidative multilayer during the polymerization (**Figure 9a**). In contrast, DHI-melanin forms mainly on the outer surface of the oxidative film. $(PP/Ce/rGO/Ce)_{15}$/(DHI-melanin) film is approximately 270 nm thick, as roughly estimated by custom-made scanning white light interferometer[155] (SWLI, **Figure 10**) (see **article III** for details). Essentially, SWLI is optical interference type method, which is suitable for the approximation of the dimensions of craters created by argon gas cluster sputtering.

The root-mean-square (rms) surface roughness of the films was approximated with *ex situ* atomic force microscopy (*ex situ* AFM, from 10 µm x 10 µm images, **Figure 9c,d** and **articles II, III**) and the results for the $(PP/Ce/GO/Ce)_n$ and $(PP/Ce/GO/Ce)_n$/PEDOT films are shown in the inset of **Figure 9a**. The rms surface roughness of the spin-spray $(PP/Ce/GO/Ce)_n$ and $(PP/Ce/GO/Ce)_n$/PEDOT films levels off from $n \geq 10$ and the films are much smoother than the corresponding oxidative dip-LbL films[113]. Graphene oxide sheets are clearly visible in the *ex situ* AFM image of the thinnest $(PP/Ce/GO/Ce)_3$/PEDOT film (**Figure 9c**) but PEDOT obscures the sheets in the thicker films (**Figure 9d,e**). Finally, the rms surface roughness of the spin-spray $(PP/Ce/(r)GO/Ce)_{15}$/(DHI-melanin) film was approximately 19 nm, in line with $(PP/Ce/GO/Ce)_n$ and $(PP/Ce/GO/Ce)_n$/PEDOT films (see **article III** for details). Overall, both the linear growth and the surface roughness leveling imply that the spin-spray $(PP/Ce/GO/Ce)_n$ multilayers have a stratified structure with more or less distinct layers.

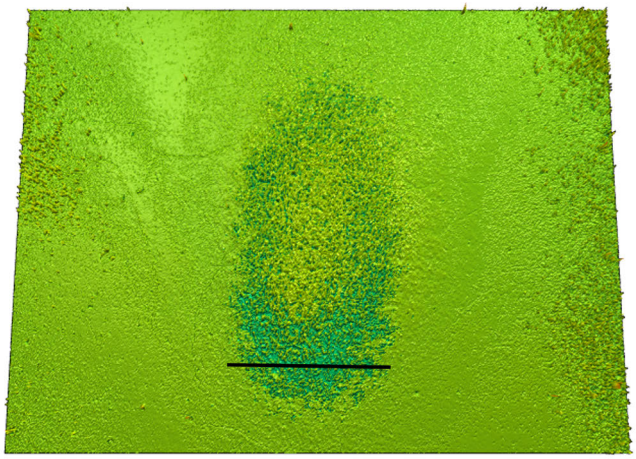

Figure 10. 3D scanning white light interferometry image of the $(PP/Ce/rGO/Ce)_{15}$/(DHI melanin) film. Film thickness was estimated from the deepest part of the crater (black line).[**article III**]

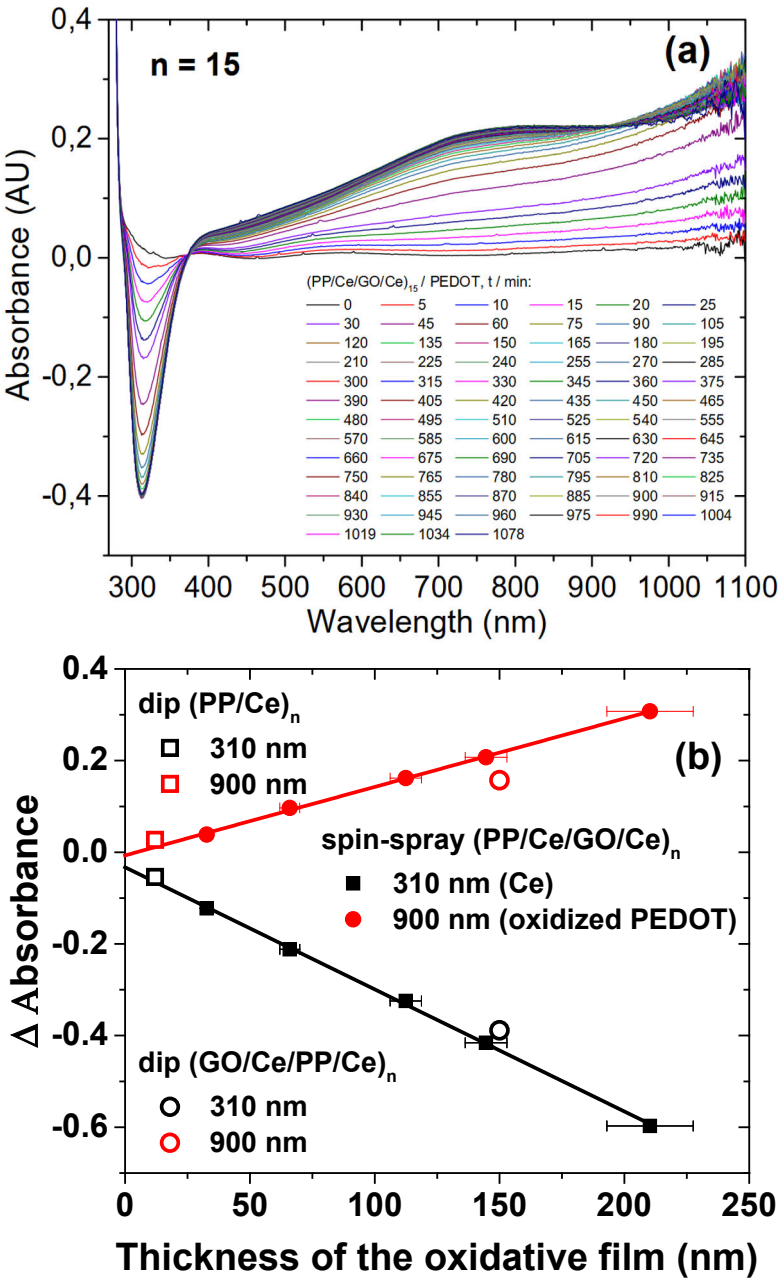

Figure 11. **(a)** Polymerization of 10 mM EDOT onto the $(PP/Ce/GO/Ce)_{15}$ film at pH = 1.5 as a function of time. The UV-Vis spectrum of the oxidative $(PP/Ce/GO/Ce)_{15}$ film has been subtracted from the spectra. **(b)** Total absorbance change due to polymerization of PEDOT at 310 nm (black) and 900 nm (red) as a function of the thickness of the oxidative film. The absorbance changes correspond to the loss of cerium and the formation of oxidized PEDOT respectively. Lines are linear fits to the data. The data of dip-LbL films in **Figure 11b** is from our earlier work.[112,113] (a): [**article II**]; (b): [**article II**, modified image].

The amount of Ce(IV) in the $(PP/Ce/GO/Ce)_n$ is the limiting factor in the surface polymerization process onto the films. Therefore, we compared the relative amount of cerium in oxidative films by measuring the absorbance changes at 310 nm during the polymerization. Further, absorbance changes at 900 nm are proportional to the amount of as-formed PEDOT. **Figure 11** shows that they both depend linearly on the thickness of the oxidative multilayer and the values are practically independent of the oxidative film preparation method. Additionally, kinetics of Ce dissolution and PEDOT formation were similar with spin-spray $(PP/Ce/GO/Ce)_{15}$ and dip $(GO/Ce/PP/Ce)_4$[113] films of similar thickness (see **article II** and references within for details).

In conclusion, oxidative spin-spray $(PP/Ce/GO/Ce)_n$ films are more organized and smoother compared with the corresponding dip-LbL films and their build-up time is shorter. The major and somewhat unexpected result of the work was that the cerium capacity and the oxidation kinetics were nonetheless unaffected by the assembly technique when comparing films of similar thickness.

2.2.3 Electrochemical properties of spin-spray $(PP/Ce/GO/Ce)_n$/PEDOT films

The high-resolution XPS spectra of $(PP/Ce/GO/Ce)_{15}$/PEDOT film are in accordance with that of a PEDOT polymer, and thus they are omitted from this summary (see **article III** and references within). Further, *in situ* UV-Vis spectra of the $(PP/Ce/(r)GO/Ce)_n$/PEDOT films were typical for the PEDOT-based material (see **article II** and references within). Therefore, the results indicate that the structure of the polymer is as expected for a typical PEDOT polymer.

$(PP/Ce/GO/Ce)_n$/PEDOT films were studied electrochemically before and after the electrochemical reduction of GO. The reduction of GO is irreversible and can be carried out by cyclic voltammetry (CV) in cathodic potentials. Cyclic voltammograms of the $(PP/Ce/(r)GO/Ce)_n$/PEDOT electrode are nearly rectangular-shaped, which is typical for a capacitive behavior (**Figure 12a** and **articles II, III**). The integrated areal capacitance of the films (in the –0.2 V to +0.6 V *vs* Ag/AgCl potential range) is nearly linearly dependent on the film thickness in the investigated thickness range and the volumetric capacitance reaches promising values of 120-140 F/cm^3 for a PEDOT-based material (**Figure 12c,d**).[49–51] The reduction of GO increases the capacitance only slightly, which is understandable because the relative amount of graphene oxide in the films is quite small. Cycling stability of the $(PP/Ce/GO/Ce)_{15}$/PEDOT film is high, with ca. 80 % of capacitance remaining after 4000 cycles (**Figure 12b)**, which is comparable to many other PEDOT-based films[156–159].

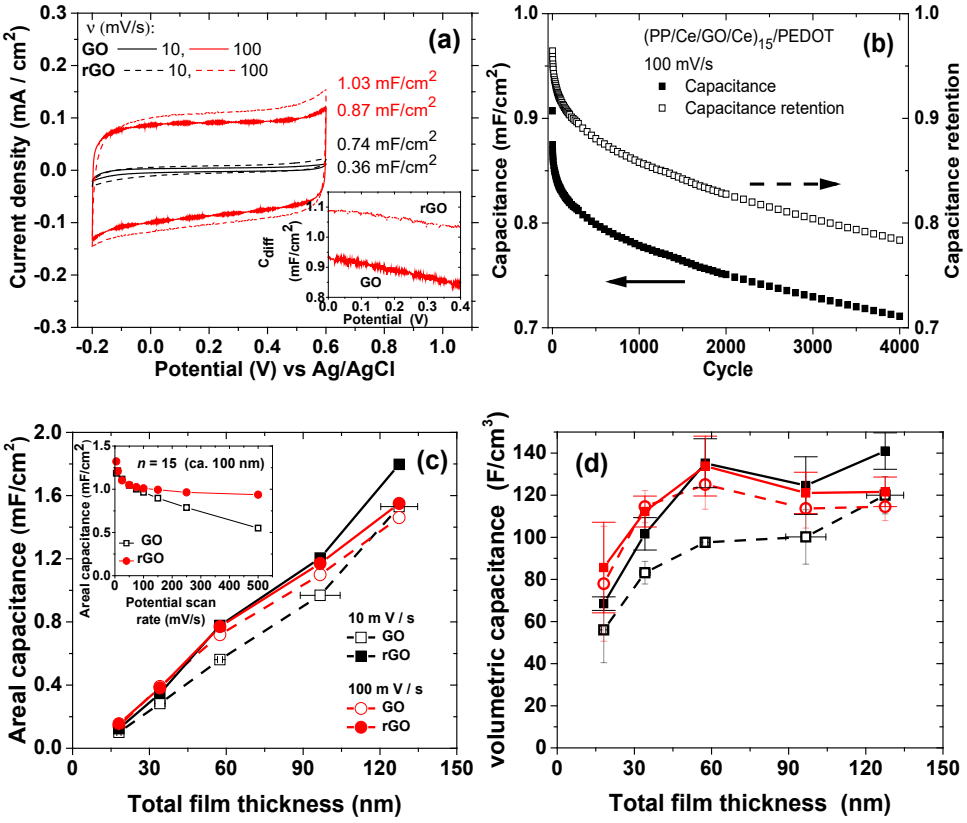

Figure 12. (a) Cyclic voltammograms of the (PP/Ce/(r)GO/Ce)$_{15}$/PEDOT electrode in 0.5 M Na_2SO_4 solution and the integrated capacitance values obtained from the CVs. Inset: the differential capacitance as a function of potential at 100 mV/s sweep rate. **(b)** Cycling performance of the (PP/Ce/GO/Ce)$_{15}$/PEDOT electrode at 100 mV/s. **(c)** Areal and **(d)** volumetric capacitance of the (PP/Ce/(r)GO/Ce)$_n$/PEDOT film as a function of film thickness. Inset in **(c)**: areal capacitance of the (PP/Ce/(r)GO/Ce)$_{15}$/PEDOT electrode as a function of scan rate. Additional details for (c) and (d) are given in **article II**. All measurements have been taken in three-electrode configuration *vs* Ag/AgCl reference electrode. (a),(b): [**article III**]; (c),(d): [**article II**, modified image].

We used electrochemical impedance (EIS) and capacitance spectroscopies to identify the various dynamic processes that contribute to the electrochemical behavior of the (PP/Ce/(r)GO/Ce)$_{15}$/PEDOT films. The real (C') and imaginary (C'') parts of the complex capacitance are obtained from the impedance data according to equations (8), where $Z' = Z'_{obs} - R_s$ (R_s = solution and electrode resistance).[160,161] C' is related to the film capacitance and C'' to conductivity and energy loss terms.[162]

$$C' = -\frac{Z''}{2\pi f|Z|^2} \qquad C'' = \frac{Z'}{2\pi f|Z|^2} \tag{8}$$

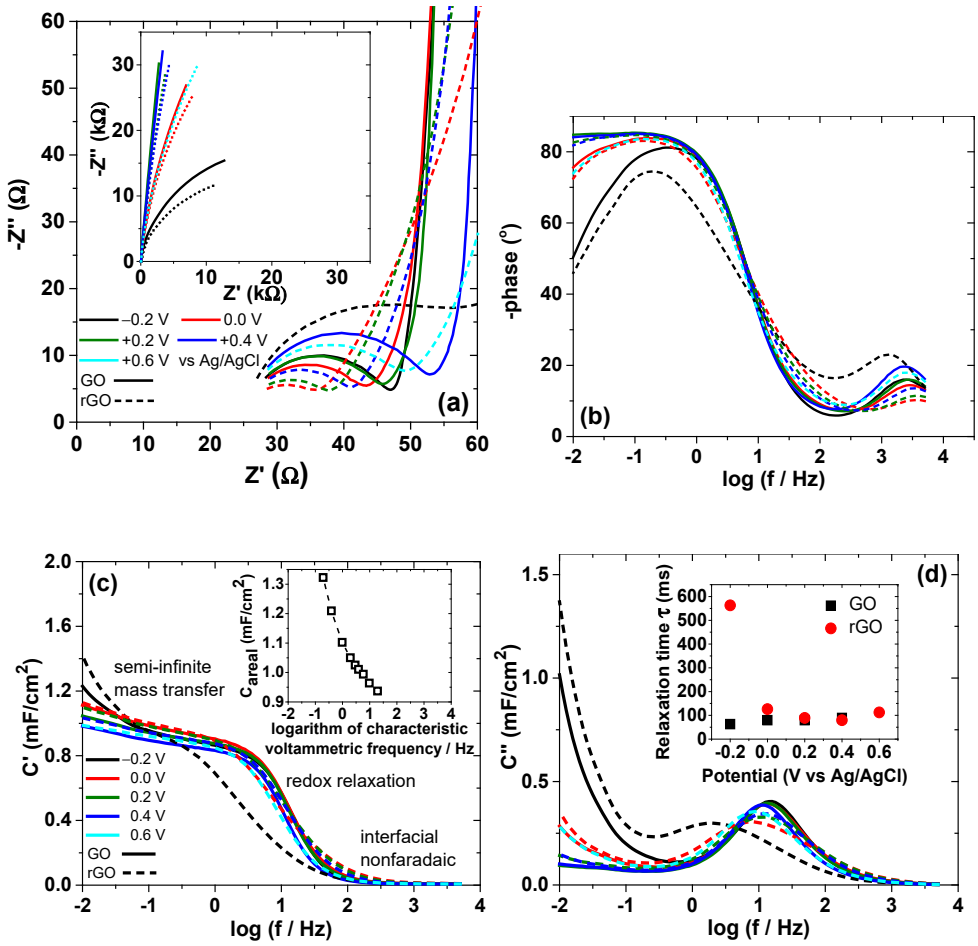

Figure 13. Impedance and complex capacitance plots of the $(PP/Ce/(r)GO/Ce)_{15}$/PEDOT electrode in 0.5 M Na_2SO_4 solution at different potentials. All measurements have been taken in three-electrode configuration *vs* Ag/AgCl reference electrode. **(a)** High frequency part of the Nyquist impedance plots (the whole frequency range is shown in the inset). **(b)** Bode plots. Real **(c)** and imaginary **(d)** parts of the complex capacitance as a function of frequency. The processes contributing to the film capacitance in different time domains are schematically shown in (c). Inset in (c) shows integrated areal capacitance of the $(PP/Ce/rGO/Ce)_{15}$/PEDOT film (cf. inset in **Figure 12c**) as a function of the inverse of the voltammetric timescale to approximately compare voltammetric and impedance results. Inset in (d) shows the relaxation time corresponding to the frequency of local maximum in different potentials. (a),(c),(d): [**article III**]; (b): [**article III**, modified image].

Electrochemical impedance and capacitance spectra of the $(PP/Ce/(r)GO/Ce)_{15}$/PEDOT film are shown in **Figure 13** and their interpretation can be summarized as follows (see **article III** and references within for details). Interfacial capacitance, redox pseudocapacitance and mass transfer effects contribute to the film capacitance at different timescales (**Figure 13c**).

- The small interfacial capacitance is effective at high frequencies. Semicircles in the Nyquist plots and humps in the Bode plots at these frequencies are attributed to the interfacial non-faradaic phenomena.
- The main contribution to the capacitance at voltammetric timescale[163] ($\frac{RT}{Fv}$, see inset in **Figure 13c**) comes from redox processes. Therefore, they cause the ultimate limitation for the power density of the films. The time constant $\tau = \frac{1}{f(C''_{max})}$ corresponding to the frequency of local maximum of C'' can be used as a figure of merit for supercapacitors because it is directly related to the power density of the capacitor.[160,164–166] Excluding the rGO-containing film at the –0.2 V potential, the average time constant is 90 ms, with a standard deviation of 20 ms, which is very small compared with many other films based on carboneous materials or polythiophenes and their composites.[160,165–171]
- The phase angle of the (PP/Ce/(r)GO/Ce)$_{15}$/PEDOT film at low frequencies is near the ideal value of –90° for pseudocapacitive materials.[172] The reduction of GO slightly increases the nonideal behavior of the film, which we attribute to the morphological changes in the porous electrode structure.[172,173] C' is of the order of 1 mF/cm^2 at low frequencies, in line with the integrated capacitance values. C' decreases slightly with potential, which is in line with differential capacitance (**Figure 12a**), but overall, the effects of potential and the reduction of GO are both very small (excluding the lowest -0.2 V potential where the conductivity of the film is low).

2.2.4 The structure and the capacitance of the spin-spray (PP/Ce/GO/Ce)$_n$/(DHI-melanin) films

The (PP/Ce/GO/Ce)$_{15}$/(DHI-melanin) film was sputtered with argon gas cluster ion beam with 4 eV cluster energy per atom to remove adventitious carbon and other impurities from the film surface. Unlike monatomic Ar^+ sputtering, the more recently introduced argon cluster sputtering minimizes the chemical changes of polymeric materials during the process.[150,151] The as-obtained high resolution XPS spectra from the film are shown in **Figure 14**.

The C 1s spectrum (**Figure 14a**) can be deconvoluted with seven peaks corresponding to C–C/C=C, C–N, C–O, C=O, COOH, and COO^- carbons, and a satellite peak. Such a fit is justified by several reasons. First of all, the binding energies are generally in line with other studies.[102,151,174] Secondly, the ratios of carbon functionalities are close to those expected, e.g., close to the DHI$_3$/(pyrrole-2,3-dicarboxylic acid) tetramer (**Table 1**)[31,71]. Finally, there is good accordance

between the relative areas of the carbon–nitrogen and carbon–oxygen peaks in the C 1s, O 1s and N 1s spectra (**Table 1**). COOH groups form in DHI-melanin by the catechol ring cleavage, and these groups bind Na^+ ions to the film from the adjacent monomer solution[63]. The O 1s spectrum (**Figure 14b**) can be deconvoluted with four peaks corresponding to C=O and C–O oxygens,[102,151,174] Na Auger peak and satellite peak. About half of the DHI-melanin is in the oxidized form according to the XPS spectrum.

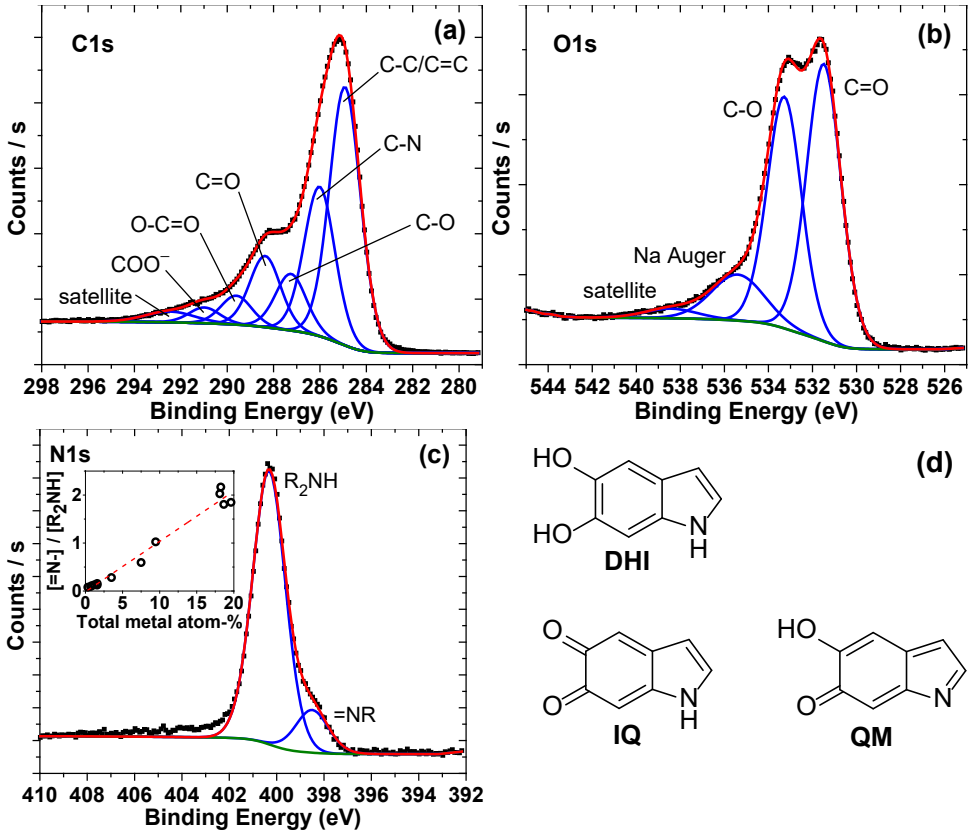

Figure 14. (a-c) The C 1s, O 1s and N 1s region XPS spectra of the $(PP/Ce/GO/Ce)_{15}$/(DHI-melanin) film after the argon gas cluster sputtering (40 s, 4 eV per atom). Inset in (c) shows the dependence of the imine/amine ratio ([=N-] / [R_2NH]) on the total metal atom-% (Ce + Na) in the film and linear fit to the data. **(d)** Structures of 5,6-dihydroxyindole (DHI), its oxidized form 5,6-indolequinone (IQ) and the tautomer of IQ: quinone methide (QM). (a)–(c): [**article III**]; (d): [**article III**, modified image].

Based on theoretical calculations[175,176] and thermodynamic considerations,[177] 5,6-dihydroxyindole (DHI), its oxidized form 5,6-indolequinone (IQ), and its tautomeric form quinone methide (QM) are assumed to be the main reduced and

oxidized forms of the as-studied DHI-melanin (**Figure 14d**, see **article III** and references within for details). The N 1s spectrum (**Figure 14c**) can be deconvoluted with two peaks. They correspond to the pyrrolic nitrogen (R-NH-R) in the indole structure[102,151,174] and to the =NR (imine group)[88,151,174] in DHI-melanin. Metal-ion binding likely influences the imine formation in DHI-melanin[61,175,178,179] and the depth profiling data allows us to test this hypothesis. The observed [=N–]/[R_2NH] ratio increases roughly linearly with sodium, cerium and total (Na + Ce) cation concentrations (see inset in **Figure 14c** and **article III**), but the imine/amine ratio is nonzero even when no metal is present. We attribute the nonzero value to the QM tautomeric form and the increase in the imine/amine ratio upon metal content to the metal-coordination-induced imine structure formation in DHI.

Table 1. The fitted C 1s, O 1s and N 1s region XPS peak parameters of the $(PP/Ce/GO/Ce)_{15}$/(DHI-melanin) film after the argon gas cluster sputtering (40 s, 4 eV per atom). DHI_3PDCA and its oxidized form IQ_3PDCA are examples of DHI-melanin oligomer structures.[**article III**, modified version]

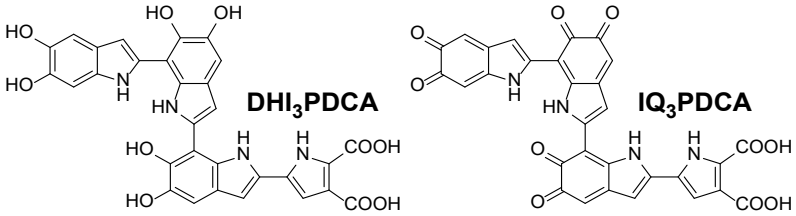

Peak	Assign-ment	Binding energy (eV)	FWHM (eV)	Normalized peak area	Atomic conc. (%)	Carbon functionalities in DHI_3PDCA/ IQ_3PDCA[1] (%)
(1) C 1s	C–C/C=C	284.9	1.6	941.5	44.5	46.7
(2) C 1s	C–N	286.0	1.6	545.0	25.8	26.7
(3) C 1s	C–O	287.3	1.6	206.6	9.8	10.0
(4) C 1s	C=O	288.4	1.6	260.0	12.3	10.0
(5) C 1s	O–C=O	289.6	1.6	105.8	5.0	6.7[2]
(6) C 1s	COO^-	291.0	1.6	57.6	2.7	
(7) C 1s	Satellite	292.5	2.5			
(1) O 1s	C=O	531.5	1.8	356.2	54.5	
(2) O 1s	C–O	533.3	1.8	298.0	45.6	
(3) O 1s	Na Auger	535.4	2.8			
(4) O 1s	Satellite	538.4	2.8			
(1) N 1s	R_2NH	400.3	1.6	266.1	86.5	
(2) N 1s	=NR	398.5	1.6	41.5	13.5	

1. Calculated values for the tetramer structure with equimolar amount of 5,6-dihydroxyindole (DHI) and 5,6-indolequinone (IQ) redox states. 2. O–C=O/COO^-

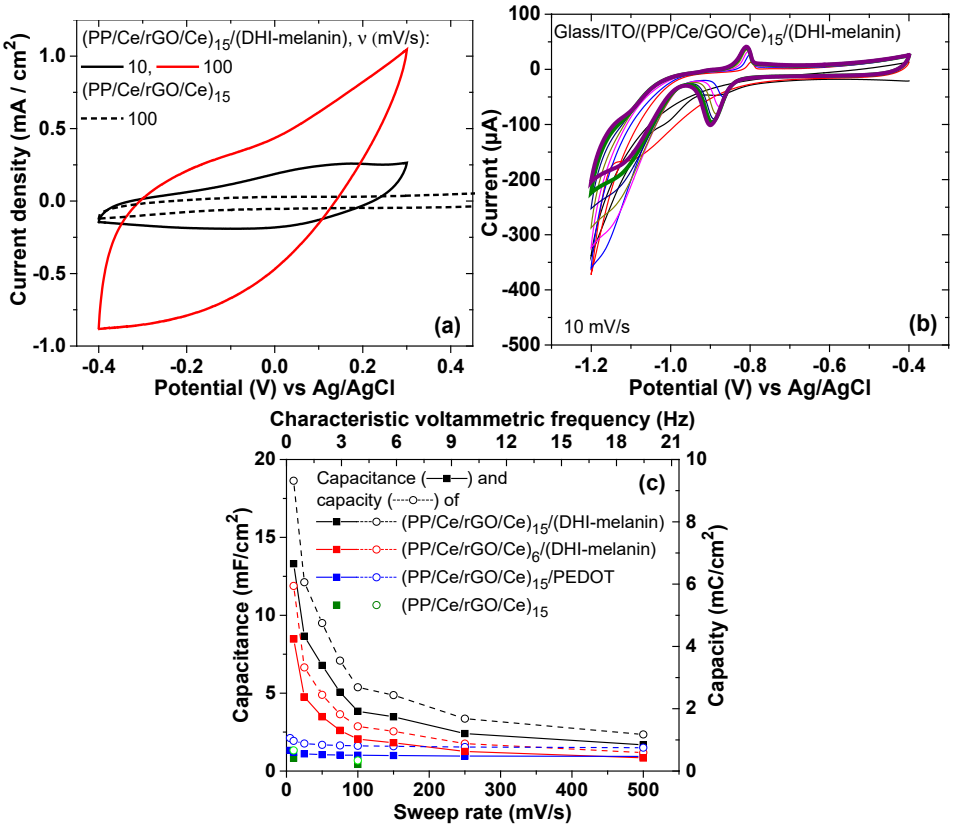

Figure 15. (a) The cyclic voltammograms of the $(PP/Ce/rGO/Ce)_{15}$ (in 0.5 M Na_2SO_4) and $(PP/Ce/rGO/Ce)_{15}$/(DHI-melanin) films (in 0.1 M phosphate buffer with 0.5 M Na_2SO_4, pH = 7.1). **(b)** The electrochemical reduction of graphene oxide in the $(PP/Ce/GO/Ce)_{15}$/(DHI-melanin) film. Last two cycles are highlighted. **(c)** The integrated capacitance and the charge storage capacity of the $(PP/Ce/rGO/Ce)_{15}$, $(PP/Ce/rGO/Ce)_{15}$/PEDOT and $(PP/Ce/rGO/Ce)_{6 \text{ or } 15}$/(DHI-melanin) films with different sweep rates (first two films: estimated in the intermediate –0.2 V to +0.6 V *vs* Ag/AgCl potential range, cf. **Figure 12c**). All measurements have been taken in three-electrode configuration vs Ag/AgCl reference electrode. (a)–(c): [**article III**].

$(PP/Ce/GO/Ce)_n$/(DHI-melanin) films were reduced electrochemically (**Figure 15b**) and their cyclic voltammograms are shown in **Figure 15a** (see **article III** for additional voltammograms). Preliminary work prior to this thesis suggested that the reduction of GO significantly enhances the capacitance of the films and thus $(PP/Ce/GO/Ce)_n$/(DHI-melanin) films were not studied electrochemically in this work. The cyclic voltammograms in **Figure 15a** are rather featureless (–0.4 V to +0.3 V potential range) but a clear redox peak pair was observed at ca. –0.85 V during the electrochemical reduction of GO (**Figure 15b**), attributed to the Ce(III)/Ce(IV)–DHI-melanin complexes[180,181]. The integrated areal capacitance and capacity of the $(PP/Ce/rGO/Ce)_n$/(DHI-melanin) films are compared to the

corresponding $(PP/Ce/rGO/Ce)_{15}$/PEDOT and $(PP/Ce/rGO/Ce)_{15}$ films in **Figure 15c**. Of the films based on similar oxidative multilayers, the DHI-melanin-based film displays clearly the highest values, especially at low sweep rates. In addition, the volumetric capacitance of the $(PP/Ce/rGO/Ce)_{15}$/(DHI-melanin) is approximately 490 F/cm^3 at 10 mV/s sweep rate, about four times the value estimated for the corresponding $(PP/Ce/rGO/Ce)_{15}$/PEDOT film. However, the dynamic properties of the $(PP/Ce/rGO/Ce)_n$/(DHI-melanin) films are not optimal, and typically for melanin-based electrodes,[24,182] both the areal capacitance and capacity of the $(PP/Ce/rGO/Ce)_n$/(DHI-melanin) films decrease markedly with the sweep rate. Although the rGO can act as an electron mediator in the $(PP/Ce/rGO/Ce)_n$/(DHI-melanin) films, their structure is not optimal for the target application. More uniform depth profile would be desirable, as a partially intact oxidative multilayer weakens the electrical contact between the ITO surface and the redox-active melanin-type film, thereby increasing the time constant for electrochemical processes.

Overall, melanin-based materials have a good potential as materials for biodegradable and biocompatible charge storage. However, their conductivity needs to be increased and a promising approach for future studies is to blend them with electronically conducting materials.

3 Summary and outlook

The focus points of this thesis were (1) the study of synthetic eumelanin analogs polydopamine and DHI-melanin, (2) the preparation of oxidative multilayer films and their use for the fabrication of electroactive conducting polymer and melanin-type films.

3.1 The oxidation of dopamine to polydopamine

First of all, we studied the pH-dependence of the autoxidation of dopamine to polydopamine, a well-known synthetic eumelanin analog. The critical initial steps in the Raper-Mason reaction pathway of dopamine to polydopamine are (1) the one-electron oxidation of dopamine to dopaminesemiquinone and its subsequent reaction to dopaminequinone, and (2) the intramolecular cyclization of dopaminequinone to leucodopaminechrome. The classical method for the polydopamine fabrication is to dissolve dopamine in the basic aqueous solution and allow O_2 to act as an oxidant (autoxidation). By using thermodynamic analysis and experimental studies, we were able to show that the leucodopaminechrome formation rate begins to accelerate already above pH 5 but strong acceleration is observed not until at much higher pH 8–9. Leucodopaminechrome reacts further to eventually yield polydopamine. The decisive physicochemical parameters that control the autoxidation of dopamine are the pK_a value of the hydroxyl group in the semiquinone radical (ca. 4.7) and the pK_a value of the protonated amino group in the dopaminequinone (ca. 9.6).

Secondly, we studied the oxidation of dopamine to polydopamine at different pHs in the presence of three redox active transition metal ions: the widely used strong Ce(IV) oxidant and redox active biometals Fe(III) and Cu(II). All these ions lower the onset pH of dopamine oxidation significantly. The oxidation power of Ce(IV) and Fe(III) ions increases with decreasing pH and both can oxidize dopamine to dopaminesemiquinone in the anaerobic conditions at acidic pH. However, the lightly acidic pH (e.g. 4.5) is optimal for the polydopamine synthesis since the intramolecular cyclization of dopaminequinone becomes rate-determining at low pH. Interestingly, our calculations show that Cu(II) is not as strong oxidant as Ce(IV) and Fe(III) in the strongly acidic pH, but in the presence of chloride ions, it is a better

oxidant from pH 5 upwards (including the physiological pH 7.4). Chloride ions increase the formal potential of Cu(II)/Cu(I) due to the formation of Cu(I)-chloro complexes.

3.2 Oxidative multilayer films

As a second topic in the thesis, we studied the oxidative layer-by-layer (LbL) films composed of polyphosphate (PP), graphene oxide (GO) and Ce(IV)/Ce(III) ions: $(PP/Ce/GO/Ce)_n$. They have been shown to be a general platform for the oxidative generation of electroactive conducting polymer and melanin-type films. In this work, we studied especially the production of the oxidative multilayers and their use for the fabrication of thin electroactive films.

In essence, the multilayer films with mobile oxidant (e.g. Ce(IV)) and coordinative binder (e.g. PP) can oxidize monomers from the adjacent solution onto the film structure. The addition of graphene oxide in the $(PP/Ce)_n$ films significantly improves their growth, which is important for their practical applicability. However, the preparation of thick dip-LbL $(GO/Ce/PP/Ce)_n$ films is still slow, their morphology is not well defined and their surface roughness is very high. Therefore, in order to improve the production and properties of the films, we studied the preparation of oxidative films with more advanced, automated spin-spray layer-by-layer assembly method. The spin-spray-LbL $(PP/Ce/GO/Ce)_n$ films have a stratified structure, their assembly time is shorter (under a minute per layer), and their surface roughness is low. Finally, their thickness increases linearly with the number of tetralayers (ca. 11 nm/tetralayer) and can thus be precisely controlled.

By utilizing a modern X-ray photoelectron spectrometer with an argon gas cluster depth profiling, we were able to study the operating principle of the oxidative multilayers and the structure of the functional films in detail. The coordinative binder polyphosphate has a central role in the operation. It degrades hydrolytically in acidic aqueous solutions and thus the oxidative film can be dissolved in the surrounding solution during the polymer film fabrication. In this way, we were able to fabricate GO/PEDOT film with ca. 80 % w/w PEDOT by using a long polymerization time (17 h) and low pH (1.5). The process can be accelerated significantly if desired, since based on the UV-Vis absorbance the Ce(IV) ions have almost completely disappeared from the film in two hours with $(PP/Ce/GO/Ce)_{15}$/PEDOT film. On the other hand, as shown by high-resolution XPS analysis and depth profiling, DHI-melanin grows mainly on top of the oxidative film during a 2 h synthesis at pH 4.5. In this case, it is not possible to use arbitrary long reaction times due to competing self-aggregation of DHI-melanin in the solution phase. However, it would be interesting to study if DHI-melanin can be oxidized onto the oxidative films at acidic pH in order to remove the oxidative film from the structure. Graphene oxide

in the DHI-melanin-based films can be reduced to electronically conductive rGO after the polymerization processes, which enhances the electroactivity of the DHI-melanin-based films significantly.

The primary goal of the research was to provide knowledge on materials that can be potentially used as electrode materials in biocompatible and/or biodegradable supercapacitors. Therefore, we studied the electrochemical properties of thin $(PP/Ce/GO/Ce)_n$/PEDOT and $(PP/Ce/GO/Ce)_n$/(DHI-melanin) films in a three-electrode configuration. Capacitance and charge transfer kinetics of the PEDOT-based films were both promising. Thin PEDOT-based films reached promising 120-140 F/cm^3 capacitance values. By using electrochemical impedance and capacitance spectroscopies, we demonstrated that the main contribution to the capacitance comes from redox processes. Therefore, they ultimately limit the power density of the films. Bioinspired DHI-melanin-based films reached even more promising areal and volumetric capacitances. However, in line with the literature, the dynamic properties of the melanin-based electrodes were not optimal and studied films in fact had an undesired nonuniform depth profile. Both the fabrication methods and the conductivity of melanin-based materials need to be enhanced and the latter can be achieved by blending more electronically conductive material to the films.

In conclusion, oxidative multilayers do not appear to be optimal for the preparation of DHI-melanin films but produce high quality PEDOT-based films. However, our results indicate that DHI-melanin is a promising component for biodegradable supercapacitors. New film formation techniques need to be developed in order to achieve its full potential. Notably, chemically similar films can also be obtained by the oxidation of dopamine under suitable conditions.

This work provides an excellent starting point for more application-oriented studies of oxidative multilayer films. In the future work, the assembly time of the oxidative films can be most likely improved by optimizing the film assembly parameters (here, the individual layers were assembled with intentionally slow and safe parameters: reagent spraying = 3 s, drying = 20 s, rinsing = 10 s, drying 20 s). It would also be interesting to study the fabrication of oxidative films with a simpler spray-LbL assembly, preferably on a slowly rotating substrate to avoid drip patterns. This method is more suitable for large, industrial scale applications. Finally, a natural extension of the work is to utilize other chemically reactive metal ions in the oxidative films in addition to bioincompatible Ce(IV), like Fe(III) and Cu(II) biometals used in the oxidation of dopamine. Ce(IV) and Fe(III) are both strong oxidants at acidic pH, but Ce(IV) is stronger of these two and thus it was used in this thesis. On the other hand, Cu(II) is better oxidant than Ce(IV) and Fe(III) in neutral and basic media.

Acknowledgements

The experimental work in this thesis was carried out in the group of Physical Chemistry, Department of Chemistry, University of Turku. The funding from The Emil Aaltonen Foundation; University of Turku, Department of Chemistry; The Finnish Cultural Foundation and Foundation of Finnish Chemistry Congress and travel grants from Doctoral Programme in Physical and Chemical Sciences (PCS) and University of Turku Joint Research Grant Fund are gratefully acknowledged. I thank my pre-examiners Doctor Klemen Pirnat and Professor Tomi Laurila and opponent Associate Professor Radosław Mrówczyński for your time spent with my thesis.

I would like to express my deepest gratitude for my supervisors Professor Jukka Lukkari, Adjunct Professor Mikko Salomäki and Doctor Henri Kivelä for all your time, expertise, patience, and support over the years. I want to also thank all co-authors of my articles Ermei Mäkilä, Jarkko Leiro, Johan Nyman, Jukka Hassinen, Matti Tupala, Sari Granroth and Tuomo Ouvinen for your invaluable contribution. I also thank Adefunke Koyejo, Lippo Lassila, Milla Suominen and Sachin Kochrekar for your participation.

I am grateful for my Master's Thesis experimental work supervisor Antti Viinikanoja who helped me along the way. The work would not have been possible without the custom-made instruments by Mauri Nauma or dedicated IT support from Kari Loikas. Finally, I equally thank all my co-workers in the Department of Chemistry for making this work an unforgettable experience.

My special thanks to my parents Irene and Erkki for all the support, my brother Aarne for scientific advice and my beloved wife Henna for standing by my side and supporting me through everything. Thank you to my daughter Kaisa for bringing joy and meaning to my life.

15.11.2022

Lauri Marttila

List of References

(1) Forti, V.; Baldé, C. P.; Kuehr, R.; Bel, G. *The Global E-Waste Monitor 2020: Quantities, Flows and the Circular Economy Potential*; United Nations University/United Nations Institute for Training and Research, International Telecommunication Union, and International Solid Waste Association: Bonn, Geneva and Rotterdam, 2020.

(2) Li, R.; Wang, L.; Kong, D.; Yin, L. Recent Progress on Biodegradable Materials and Transient Electronics. *Bioact. Mater.* **2018**, *3* (3), 322–333. https://doi.org/10.1016/j.bioactmat.2017.12.001.

(3) Cao, Y.; Uhrich, K. E. Biodegradable and Biocompatible Polymers for Electronic Applications: A Review. *J. Bioact. Compat. Polym.* **2019**, *34* (1), 3–15. https://doi.org/10.1177/0883911518818075.

(4) Jia, X.; Wang, C.; Lee, C.-Y.; Yu, C.; Wallace, G. G. Energy Materials for Transient Power Sources. *MRS Bull.* **2020**, *45* (2), 121–128. https://doi.org/10.1557/mrs.2020.23.

(5) Hosseini, E. S.; Dervin, S.; Ganguly, P.; Dahiya, R. Biodegradable Materials for Sustainable Health Monitoring Devices. *ACS Appl. Bio Mater.* **2021**, *4* (1), 163–194. https://doi.org/10.1021/acsabm.0c01139.

(6) Cha, G. D.; Kang, D.; Lee, J.; Kim, D. Bioresorbable Electronic Implants: History, Materials, Fabrication, Devices, and Clinical Applications. *Adv. Healthc. Mater.* **2019**, *8* (11), 1801660. https://doi.org/10.1002/adhm.201801660.

(7) Jiang, D.; Shi, B.; Ouyang, H.; Fan, Y.; Wang, Z. L.; Li, Z. Emerging Implantable Energy Harvesters and Self-Powered Implantable Medical Electronics. *ACS Nano* **2020**, *14* (6), 6436–6448. https://doi.org/10.1021/acsnano.9b08268.

(8) Boehler, C.; Aqrawe, Z.; Asplund, M. Applications of PEDOT in Bioelectronic Medicine. *Bioelectron. Med.* **2019**, *2* (2), 89–99. https://doi.org/10.2217/bem-2019-0014.

(9) He, H.; Zhang, L.; Guan, X.; Cheng, H.; Liu, X.; Yu, S.; Wei, J.; Ouyang, J. Biocompatible Conductive Polymers with High Conductivity and High Stretchability. *ACS Appl. Mater. Interfaces* **2019**, *11* (29), 26185–26193. https://doi.org/10.1021/acsami.9b07325.

(10) Asplund, M.; Thaning, E.; Lundberg, J.; Sandberg-Nordqvist, A. C.; Kostyszyn, B.; Inganäs, O.; von Holst, H. Toxicity Evaluation of PEDOT/Biomolecular Composites Intended for Neural Communication Electrodes. *Biomed. Mater.* **2009**, *4* (4), 045009. https://doi.org/10.1088/1748-6041/4/4/045009.

(11) Chen, X.; Villa, N. S.; Zhuang, Y.; Chen, L.; Wang, T.; Li, Z.; Kong, T. Stretchable Supercapacitors as Emergent Energy Storage Units for Health Monitoring Bioelectronics. *Adv. Energy Mater.* **2020**, *10* (4), 1902769. https://doi.org/10.1002/aenm.201902769.

(12) Manjakkal, L.; Pullanchiyodan, A.; Yogeswaran, N.; Hosseini, E. S.; Dahiya, R. A Wearable Supercapacitor Based on Conductive PEDOT:PSS-Coated Cloth and a Sweat Electrolyte. *Adv. Mater.* **2020**, *32* (24), 1907254. https://doi.org/10.1002/adma.201907254.

(13) Song, W.; Zhu, J.; Gan, B.; Zhao, S.; Wang, H.; Li, C.; Wang, J. Flexible, Stretchable, and Transparent Planar Microsupercapacitors Based on 3D Porous Laser-Induced Graphene. *Small* **2018**, *14* (1), 1702249. https://doi.org/10.1002/smll.201702249.

(14) Luan, P.; Zhang, N.; Zhou, W.; Niu, Z.; Zhang, Q.; Cai, L.; Zhang, X.; Yang, F.; Fan, Q.; Zhou, W.; Xiao, Z.; Gu, X.; Chen, H.; Li, K.; Xiao, S.; Wang, Y.; Liu, H.; Xie, S. Epidermal Supercapacitor with High Performance. *Adv. Funct. Mater.* **2016**, *26* (45), 8178–8184. https://doi.org/10.1002/adfm.201603480.

(15) Sim, H. J.; Choi, C.; Lee, D. Y.; Kim, H.; Yun, J.-H.; Kim, J. M.; Kang, T. M.; Ovalle, R.; Baughman, R. H.; Kee, C. W.; Kim, S. J. Biomolecule Based Fiber Supercapacitor for Implantable Device. *Nano Energy* **2018**, *47*, 385–392. https://doi.org/10.1016/j.nanoen.2018.03.011.

(16) Liu, Y.; Ai, K.; Liu, J.; Deng, M.; He, Y.; Lu, L. Dopamine-Melanin Colloidal Nanospheres: An Efficient Near-Infrared Photothermal Therapeutic Agent for In Vivo Cancer Therapy. *Adv. Mater.* **2013**, *25* (9), 1353–1359. https://doi.org/10.1002/adma.201204683.

(17) Bettinger, C. J.; Bruggeman, J. P.; Misra, A.; Borenstein, J. T.; Langer, R. Biocompatibility of Biodegradable Semiconducting Melanin Films for Nerve Tissue Engineering. *Biomaterials* **2009**, *30* (17), 3050–3057. https://doi.org/10.1016/j.biomaterials.2009.02.018.

(18) Jeong, Y. K.; Park, S. H.; Choi, J. W. Mussel-Inspired Coating and Adhesion for Rechargeable Batteries: A Review. *ACS Appl. Mater. Interfaces* **2018**, *10* (9), 7562–7573. https://doi.org/10.1021/acsami.7b08495.

(19) Kim, Y. J.; Wu, W.; Chun, S.-E.; Whitacre, J. F.; Bettinger, C. J. Biologically Derived Melanin Electrodes in Aqueous Sodium-Ion Energy Storage Devices. *Proc. Natl. Acad. Sci.* **2013**, *110* (52), 20912–20917. https://doi.org/10.1073/pnas.1314345110.

(20) Kim, Y. J.; Wu, W.; Chun, S.-E.; Whitacre, J. F.; Bettinger, C. J. Catechol-Mediated Reversible Binding of Multivalent Cations in Eumelanin Half-Cells. *Adv. Mater.* **2014**, *26* (38), 6572–6579. https://doi.org/10.1002/adma.201402295.

(21) Sun, T.; Li, Z.; Wang, H.; Bao, D.; Meng, F.; Zhang, X. A Biodegradable Polydopamine-Derived Electrode Material for High-Capacity and Long-Life Lithium-Ion and Sodium-Ion Batteries. *Angew. Chem. Int. Ed.* **2016**, *55* (36), 10662–10666. https://doi.org/10.1002/anie.201604519.

(22) Liu, T.; Kim, K. C.; Lee, B.; Chen, Z.; Noda, S.; Jang, S. S.; Lee, S. W. Self-Polymerized Dopamine as an Organic Cathode for Li- and Na-Ion Batteries. *Energy Environ. Sci.* **2017**, *10* (1), 205–215. https://doi.org/10.1039/C6EE02641A.

(23) Yang, L.; Guo, X.; Jin, Z.; Guo, W.; Duan, G.; Liu, X.; Li, Y. Emergence of Melanin-Inspired Supercapacitors. *Nano Today* **2021**, *37*, 101075. https://doi.org/10.1016/j.nantod.2020.101075.

(24) Kumar, P.; Di Mauro, E.; Zhang, S.; Pezzella, A.; Soavi, F.; Santato, C.; Cicoira, F. Melanin-Based Flexible Supercapacitors. *J. Mater. Chem. C* **2016**, *4* (40), 9516–9525. https://doi.org/10.1039/C6TC03739A.

(25) Liu, Z.; Zhang, H.; Eredia, M.; Qiu, H.; Baaziz, W.; Ersen, O.; Ciesielski, A.; Bonn, M.; Wang, H. I.; Samorì, P. Water-Dispersed High-Quality Graphene: A Green Solution for Efficient Energy Storage Applications. *ACS Nano* **2019**, *13* (8), 9431–9441. https://doi.org/10.1021/acsnano.9b04232.

(26) Xu, R.; Gouda, A.; Caso, M. F.; Soavi, F.; Santato, C. Melanin: A Greener Route To Enhance Energy Storage under Solar Light. *ACS Omega* **2019**, *4* (7), 12244–12251. https://doi.org/10.1021/acsomega.9b01039.

(27) Gouda, A.; Masson, A.; Hoseinizadeh, M.; Soavi, F.; Santato, C. Biosourced Quinones for High-Performance Environmentally Benign Electrochemical Capacitors via Interface Engineering. *Commun. Chem.* **2022**, *5* (1), 98. https://doi.org/10.1038/s42004-022-00719-y.

(28) Kim, D.; Zozoulenko, I. Why Is Pristine PEDOT Oxidized to 33%? A Density Functional Theory Study of Oxidative Polymerization Mechanism. *J. Phys. Chem. B* **2019**, *123* (24), 5160–5167. https://doi.org/10.1021/acs.jpcb.9b01745.

(29) Chen, C.-T.; Martin-Martinez, F. J.; Jung, G. S.; Buehler, M. J. Polydopamine and Eumelanin Molecular Structures Investigated with Ab Initio Calculations. *Chem. Sci.* **2017**, *8* (2), 1631–1641. https://doi.org/10.1039/C6SC04692D.

(30) Liebscher, J. Chemistry of Polydopamine – Scope, Variation, and Limitation. *Eur. J. Org. Chem.* **2019**, *2019* (31–32), 4976–4994. https://doi.org/10.1002/ejoc.201900445.

(31) Della Vecchia, N. F.; Avolio, R.; Alfè, M.; Errico, M. E.; Napolitano, A.; d'Ischia, M. Building-Block Diversity in Polydopamine Underpins a Multifunctional Eumelanin-Type Platform Tunable Through a Quinone Control Point. *Adv. Funct. Mater.* **2013**, *23* (10), 1331–1340. https://doi.org/10.1002/adfm.201202127.

(32) Berggren, M.; Crispin, X.; Fabiano, S.; Jonsson, M. P.; Simon, D. T.; Stavrinidou, E.; Tybrandt, K.; Zozoulenko, I. Ion Electron–Coupled Functionality in Materials and Devices Based on Conjugated Polymers. *Adv. Mater.* **2019**, *31* (22), 1805813. https://doi.org/10.1002/adma.201805813.

(33) Wen, Y.; Xu, J. Scientific Importance of Water-Processable PEDOT-PSS and Preparation, Challenge and New Application in Sensors of Its Film Electrode: A Review. *J. Polym. Sci. Part Polym. Chem.* **2017**, *55* (7), 1121–1150. https://doi.org/10.1002/pola.28482.

(34) Corradi, R.; Armes, S. P. Chemical Synthesis of Poly(3,4-ethylenedioxythiophene). *Synth. Met.* **1997**, *84* (1–3), 453–454. https://doi.org/10.1016/S0379-6779(97)80828-4.

(35) Ahonen, H. J.; Lukkari, J.; Kankare, J. n- and p-Doped Poly(3,4-ethylenedioxythiophene): Two Electronically Conducting States of the Polymer. *Macromolecules* **2000**, *33* (18), 6787–6793. https://doi.org/10.1021/ma0004312.

(36) Gueye, M. N.; Carella, A.; Faure-Vincent, J.; Demadrille, R.; Simonato, J.-P. Progress in Understanding Structure and Transport Properties of PEDOT-Based Materials: A Critical Review. *Prog. Mater. Sci.* **2020**, *108*, 100616. https://doi.org/10.1016/j.pmatsci.2019.100616.

(37) Chen, H.-W.; Li, C. PEDOT: Fundamentals and Its Nanocomposites for Energy Storage. *Chin. J. Polym. Sci.* **2020**, *38* (5), 435–448. https://doi.org/10.1007/s10118-020-2373-2.

(38) Kudoh, Y.; Akami, K.; Matsuya, Y. Solid Electrolytic Capacitor with Highly Stable Conducting Polymer as a Counter Electrode. *Synth. Met.* **1999**, *102* (1–3), 973–974. https://doi.org/10.1016/S0379-6779(98)01012-1.

(39) Pei, Q.; Zuccarello, G.; Ahlskog, M.; Inganäs, O. Electrochromic and Highly Stable Poly(3,4-ethylenedioxythiophene) Switches between Opaque Blue-Black and Transparent Sky Blue. *Polymer* **1994**, *35* (7), 1347–1351. https://doi.org/10.1016/0032-3861(94)90332-8.

(40) Kirchmeyer, S.; Reuter, K. Scientific Importance, Properties and Growing Applications of Poly(3,4-ethylenedioxythiophene). *J. Mater. Chem.* **2005**, *15* (21), 2077. https://doi.org/10.1039/b417803n.

(41) Zozoulenko, I.; Singh, A.; Singh, S. K.; Gueskine, V.; Crispin, X.; Berggren, M. Polarons, Bipolarons, And Absorption Spectroscopy of PEDOT. *ACS Appl. Polym. Mater.* **2019**, *1* (1), 83–94. https://doi.org/10.1021/acsapm.8b00061.

(42) Cho, B.; Park, K. S.; Baek, J.; Oh, H. S.; Koo Lee, Y.-E.; Sung, M. M. Single-Crystal Poly(3,4-ethylenedioxythiophene) Nanowires with Ultrahigh Conductivity. *Nano Lett.* **2014**, *14* (6), 3321–3327. https://doi.org/10.1021/nl500748y.

(43) Massonnet, N.; Carella, A.; Jaudouin, O.; Rannou, P.; Laval, G.; Celle, C.; Simonato, J.-P. Improvement of the Seebeck Coefficient of PEDOT:PSS by Chemical Reduction Combined with

a Novel Method for Its Transfer Using Free-Standing Thin Films. *J Mater Chem C* **2014**, *2* (7), 1278–1283. https://doi.org/10.1039/C3TC31674B.

(44) Zhao, Z.; Richardson, G. F.; Meng, Q.; Zhu, S.; Kuan, H.-C.; Ma, J. PEDOT-Based Composites as Electrode Materials for Supercapacitors. *Nanotechnology* **2016**, *27* (4), 042001. https://doi.org/10.1088/0957-4484/27/4/042001.

(45) Li, Q.; Horn, M.; Wang, Y.; MacLeod, J.; Motta, N.; Liu, J. A Review of Supercapacitors Based on Graphene and Redox-Active Organic Materials. *Materials* **2019**, *12* (5), 703. https://doi.org/10.3390/ma12050703.

(46) Sahalianov, I.; Singh, S. K.; Tybrandt, K.; Berggren, M.; Zozoulenko, I. The Intrinsic Volumetric Capacitance of Conducting Polymers: Pseudo-Capacitors or Double-Layer Supercapacitors? *RSC Adv.* **2019**, *9* (72), 42498–42508. https://doi.org/10.1039/C9RA10250G.

(47) Zhang, X.; Xiao, Z.; Liu, X.; Mei, P.; Yang, Y. Redox-Active Polymers as Organic Electrode Materials for Sustainable Supercapacitors. *Renew. Sustain. Energy Rev.* **2021**, *147*, 111247. https://doi.org/10.1016/j.rser.2021.111247.

(48) Snook, G. A.; Chen, G. Z. The Measurement of Specific Capacitances of Conducting Polymers Using the Quartz Crystal Microbalance. *J. Electroanal. Chem.* **2008**, *612* (1), 140–146. https://doi.org/10.1016/j.jelechem.2007.08.024.

(49) Rivnay, J.; Leleux, P.; Ferro, M.; Sessolo, M.; Williamson, A.; Koutsouras, D. A.; Khodagholy, D.; Ramuz, M.; Strakosas, X.; Owens, R. M.; Benar, C.; Badier, J.-M.; Bernard, C.; Malliaras, G. G. High-Performance Transistors for Bioelectronics through Tuning of Channel Thickness. *Sci. Adv.* **2015**, *1* (4), e1400251. https://doi.org/10.1126/sciadv.1400251.

(50) Volkov, A. V.; Wijeratne, K.; Mitraka, E.; Ail, U.; Zhao, D.; Tybrandt, K.; Andreasen, J. W.; Berggren, M.; Crispin, X.; Zozoulenko, I. V. Understanding the Capacitance of PEDOT:PSS. *Adv. Funct. Mater.* **2017**, *27* (28), 1700329. https://doi.org/10.1002/adfm.201700329.

(51) Kurra, N.; Park, J.; Alshareef, H. N. A Conducting Polymer Nucleation Scheme for Efficient Solid-State Supercapacitors on Paper. *J Mater Chem A* **2014**, *2* (40), 17058–17065. https://doi.org/10.1039/C4TA03603D.

(52) Meng, Q.; Cai, K.; Chen, Y.; Chen, L. Research Progress on Conducting Polymer Based Supercapacitor Electrode Materials. *Nano Energy* **2017**, *36*, 268–285. https://doi.org/10.1016/j.nanoen.2017.04.040.

(53) K, N.; Rout, C. S. Conducting Polymers: A Comprehensive Review on Recent Advances in Synthesis, Properties and Applications. *RSC Adv.* **2021**, *11* (10), 5659–5697. https://doi.org/10.1039/D0RA07800J.

(54) Lee, H.; Dellatore, S. M.; Miller, W. M.; Messersmith, P. B. Mussel-Inspired Surface Chemistry for Multifunctional Coatings. *Science* **2007**, *318* (5849), 426–430. https://doi.org/10.1126/science.1147241.

(55) Ryu, J. H.; Messersmith, P. B.; Lee, H. Polydopamine Surface Chemistry: A Decade of Discovery. *ACS Appl. Mater. Interfaces* **2018**, *10* (9), 7523–7540. https://doi.org/10.1021/acsami.7b19865.

(56) Kim, B. H.; Lee, D. H.; Kim, J. Y.; Shin, D. O.; Jeong, H. Y.; Hong, S.; Yun, J. M.; Koo, C. M.; Lee, H.; Kim, S. O. Mussel-Inspired Block Copolymer Lithography for Low Surface Energy Materials of Teflon, Graphene, and Gold. *Adv. Mater.* **2011**, *23* (47), 5618–5622. https://doi.org/10.1002/adma.201103650.

(57) Lee, H. A.; Park, E.; Lee, H. Polydopamine and Its Derivative Surface Chemistry in Material Science: A Focused Review for Studies at KAIST. *Adv. Mater.* **2020**, *32* (35), 1907505. https://doi.org/10.1002/adma.201907505.

(58) *Merck online store*. https://www.sigmaaldrich.com/FI/en/product/sigma/h8502 (accessed 2022-08-26).

(59) Yang, J.; Cohen Stuart, M. A.; Kamperman, M. Jack of All Trades: Versatile Catechol Crosslinking Mechanisms. *Chem Soc Rev* **2014**, *43* (24), 8271–8298. https://doi.org/10.1039/C4CS00185K.

(60) Xu, L. Q.; Yang, W. J.; Neoh, K.-G.; Kang, E.-T.; Fu, G. D. Dopamine-Induced Reduction and Functionalization of Graphene Oxide Nanosheets. *Macromolecules* **2010**, *43* (20), 8336–8339. https://doi.org/10.1021/ma101526k.

(61) Salomäki, M.; Ouvinen, T.; Marttila, L.; Kivelä, H.; Leiro, J.; Mäkilä, E.; Lukkari, J. Polydopamine Nanoparticles Prepared Using Redox-Active Transition Metals. *J. Phys. Chem. B* **2019**, *123* (11), 2513–2524. https://doi.org/10.1021/acs.jpcb.8b11994.

(62) Ryu, J.; Ku, S. H.; Lee, M.; Park, C. B. Bone-like Peptide/Hydroxyapatite Nanocomposites Assembled with Multi-Level Hierarchical Structures. *Soft Matter* **2011**, *7* (16), 7201. https://doi.org/10.1039/c1sm05307h.

(63) Hong, L.; Simon, J. D. Current Understanding of the Binding Sites, Capacity, Affinity, and Biological Significance of Metals in Melanin. *J. Phys. Chem. B* **2007**, *111* (28), 7938–7947. https://doi.org/10.1021/jp071439h.

(64) Li, S.; Yu, C.; Yang, J.; Zhao, C.; Fan, X.; Huang, H.; Han, X.; Wang, J.; He, X.; Qiu, J. Ultrathin Nitrogen-Enriched Hybrid Carbon Nanosheets for Supercapacitors with Ultrahigh Rate Performance and High Energy Density. *ChemElectroChem* **2017**, *4* (2), 369–375. https://doi.org/10.1002/celc.201600614.

(65) Kong, J.; Yee, W. A.; Yang, L.; Wei, Y.; Phua, S. L.; Ong, H. G.; Ang, J. M.; Li, X.; Lu, X. Highly Electrically Conductive Layered Carbon Derived from Polydopamine and Its Functions in SnO_2-Based Lithium Ion Battery Anodes. *Chem. Commun.* **2012**, *48* (83), 10316. https://doi.org/10.1039/c2cc35284b.

(66) Solano, F. Melanins: Skin Pigments and Much More—Types, Structural Models, Biological Functions, and Formation Routes. *New J. Sci.* **2014**, *2014*, 1–28. https://doi.org/10.1155/2014/498276.

(67) Meredith, P.; Sarna, T. The Physical and Chemical Properties of Eumelanin. *Pigment Cell Res.* **2006**, *19* (6), 572–594. https://doi.org/10.1111/j.1600-0749.2006.00345.x.

(68) Cao, W.; Zhou, X.; McCallum, N. C.; Hu, Z.; Ni, Q. Z.; Kapoor, U.; Heil, C. M.; Cay, K. S.; Zand, T.; Mantanona, A. J.; Jayaraman, A.; Dhinojwala, A.; Deheyn, D. D.; Shawkey, M. D.; Burkart, M. D.; Rinehart, J. D.; Gianneschi, N. C. Unraveling the Structure and Function of Melanin through Synthesis. *J. Am. Chem. Soc.* **2021**, *143* (7), 2622–2637. https://doi.org/10.1021/jacs.0c12322.

(69) Simon, J. D.; Peles, D. N. The Red and the Black. *Acc. Chem. Res.* **2010**, *43* (11), 1452–1460. https://doi.org/10.1021/ar100079y.

(70) d'Ischia, M.; Wakamatsu, K.; Napolitano, A.; Briganti, S.; Garcia-Borron, J.-C.; Kovacs, D.; Meredith, P.; Pezzella, A.; Picardo, M.; Sarna, T.; Simon, J. D.; Ito, S. Melanins and Melanogenesis: Methods, Standards, Protocols. *Pigment Cell Melanoma Res.* **2013**, *26* (5), 616–633. https://doi.org/10.1111/pcmr.12121.

(71) Alfieri, M. L.; Micillo, R.; Panzella, L.; Crescenzi, O.; Oscurato, S. L.; Maddalena, P.; Napolitano, A.; Ball, V.; d'Ischia, M. Structural Basis of Polydopamine Film Formation: Probing 5,6-Dihydroxyindole-Based Eumelanin Type Units and the Porphyrin Issue. *ACS Appl. Mater. Interfaces* **2018**, *10* (9), 7670–7680. https://doi.org/10.1021/acsami.7b09662.

(72) d'Ischia, M.; Napolitano, A.; Pezzella, A.; Meredith, P.; Buehler, M. Melanin Biopolymers: Tailoring Chemical Complexity for Materials Design. *Angew. Chem. Int. Ed.* **2020**, *59* (28), 11196–11205. https://doi.org/10.1002/anie.201914276.

(73) Xie, W.; Pakdel, E.; Liang, Y.; Kim, Y. J.; Liu, D.; Sun, L.; Wang, X. Natural Eumelanin and Its Derivatives as Multifunctional Materials for Bioinspired Applications: A Review. *Biomacromolecules* **2019**, *20* (12), 4312–4331. https://doi.org/10.1021/acs.biomac.9b01413.

(74) Delparastan, P.; Malollari, K. G.; Lee, H.; Messersmith, P. B. Direct Evidence for the Polymeric Nature of Polydopamine. *Angew. Chem. Int. Ed.* **2019**, *58* (4), 1077–1082. https://doi.org/10.1002/anie.201811763.

(75) Lyu, Q.; Hsueh, N.; Chai, C. L. L. Unravelling the Polydopamine Mystery: Is the End in Sight? *Polym. Chem.* **2019**, *10* (42), 5771–5777. https://doi.org/10.1039/C9PY01372E.

(76) Zangmeister, R. A.; Morris, T. A.; Tarlov, M. J. Characterization of Polydopamine Thin Films Deposited at Short Times by Autoxidation of Dopamine. *Langmuir* **2013**, *29* (27), 8619–8628. https://doi.org/10.1021/la400587j.

(77) Raper, H. S. The Tyrosinase-Tyrosine Reaction. *Biochem. J.* **1927**, *21* (1), 89–96. https://doi.org/10.1042/bj0210089.

(78) Mason, H. S. THE CHEMISTRY OF MELANIN. *J. Biol. Chem.* **1948**, *172* (1), 83–99. https://doi.org/10.1016/S0021-9258(18)35614-X.

(79) Micillo, R.; Panzella, L.; Iacomino, M.; Prampolini, G.; Cacelli, I.; Ferretti, A.; Crescenzi, O.; Koike, K.; Napolitano, A.; d'Ischia, M. Eumelanin Broadband Absorption Develops from Aggregation-Modulated Chromophore Interactions under Structural and Redox Control. *Sci. Rep.* **2017**, *7* (1), 41532. https://doi.org/10.1038/srep41532.

(80) Ponzio, F.; Barthès, J.; Bour, J.; Michel, M.; Bertani, P.; Hemmerlé, J.; d'Ischia, M.; Ball, V. Oxidant Control of Polydopamine Surface Chemistry in Acids: A Mechanism-Based Entry to Superhydrophilic-Superoleophobic Coatings. *Chem. Mater.* **2016**, *28* (13), 4697–4705. https://doi.org/10.1021/acs.chemmater.6b01587.

(81) Chen, C.-T.; Ball, V.; de Almeida Gracio, J. J.; Singh, M. K.; Toniazzo, V.; Ruch, D.; Buehler, M. J. Self-Assembly of Tetramers of 5,6-Dihydroxyindole Explains the Primary Physical Properties of Eumelanin: Experiment, Simulation, and Design. *ACS Nano* **2013**, *7* (2), 1524–1532. https://doi.org/10.1021/nn305305d.

(82) Liebscher, J.; Mrówczyński, R.; Scheidt, H. A.; Filip, C.; Hădade, N. D.; Turcu, R.; Bende, A.; Beck, S. Structure of Polydopamine: A Never-Ending Story? *Langmuir* **2013**, *29* (33), 10539–10548. https://doi.org/10.1021/la4020288.

(83) Cîrcu, M.; Filip, C. Closer to the Polydopamine Structure: New Insights from a Combined $^{13}C/^{1}H/^{2}H$ Solid-State NMR Study on Deuterated Samples. *Polym. Chem.* **2018**, *9* (24), 3379–3387. https://doi.org/10.1039/C8PY00633D.

(84) Ding, Y.; Weng, L.-T.; Yang, M.; Yang, Z.; Lu, X.; Huang, N.; Leng, Y. Insights into the Aggregation/Deposition and Structure of a Polydopamine Film. *Langmuir* **2014**, *30* (41), 12258–12269. https://doi.org/10.1021/la5026608.

(85) Dreyer, D. R.; Miller, D. J.; Freeman, B. D.; Paul, D. R.; Bielawski, C. W. Elucidating the Structure of Poly(dopamine). *Langmuir* **2012**, *28* (15), 6428–6435. https://doi.org/10.1021/la204831b.

(86) Hong, S.; Na, Y. S.; Choi, S.; Song, I. T.; Kim, W. Y.; Lee, H. Non-Covalent Self-Assembly and Covalent Polymerization Co-Contribute to Polydopamine Formation. *Adv. Funct. Mater.* **2012**, *22* (22), 4711–4717. https://doi.org/10.1002/adfm.201201156.

(87) Hong, S.; Wang, Y.; Park, S. Y.; Lee, H. Progressive Fuzzy Cation-π Assembly of Biological Catecholamines. *Sci. Adv.* **2018**, *4* (9), eaat7457. https://doi.org/10.1126/sciadv.aat7457.

(88) Lyu, Q.; Hsueh, N.; Chai, C. L. L. Direct Evidence for the Critical Role of 5,6-Dihydroxyindole in Polydopamine Deposition and Aggregation. *Langmuir* **2019**, *35* (15), 5191–5201. https://doi.org/10.1021/acs.langmuir.9b00392.

(89) Liu, Y.; Ai, K.; Lu, L. Polydopamine and Its Derivative Materials: Synthesis and Promising Applications in Energy, Environmental, and Biomedical Fields. *Chem. Rev.* **2014**, *114* (9), 5057–5115. https://doi.org/10.1021/cr400407a.

(90) Horak, V.; Weeks, G. Poly(5,6-dihydroxyindole) Melanin Film Electrode. *Bioorganic Chem.* **1993**, *21* (1), 24–33. https://doi.org/10.1006/bioo.1993.1004.

(91) Charkoudian, L. K.; Franz, K. J. Fe(III)-Coordination Properties of Neuromelanin Components: 5,6-Dihydroxyindole and 5,6-Dihydroxyindole-2-Carboxylic Acid. *Inorg. Chem.* **2006**, *45* (9), 3657–3664. https://doi.org/10.1021/ic060014r.

(92) Lyu, Q.; Song, H.; Yakovlev, N. L.; Tan, W. S.; Chai, C. L. L. *In Situ* Insights into the Nanoscale Deposition of 5,6-Dihydroxyindole-Based Coatings and the Implications on the Underwater Adhesion Mechanism of Polydopamine Coatings. *RSC Adv.* **2018**, *8* (49), 27695–27702. https://doi.org/10.1039/C8RA04472D.

(93) Reale, S.; Crucianelli, M.; Pezzella, A.; d'Ischia, M.; De Angelis, F. Exploring the Frontiers of Synthetic Eumelanin Polymers by High-Resolution Matrix-Assisted Laser/Desorption Ionization Mass Spectrometry. *J. Mass Spectrom.* **2012**, *47* (1), 49–53. https://doi.org/10.1002/jms.2025.

(94) Pezzella, A.; Panzella, L.; Natangelo, A.; Arzillo, M.; Napolitano, A.; d'Ischia, M. 5,6-Dihydroxyindole Tetramers with "Anomalous" Interunit Bonding Patterns by Oxidative Coupling of 5,5',6,6'-Tetrahydroxy-2,7'-Biindolyl: Emerging Complexities on the Way toward an Improved Model of Eumelanin Buildup. *J. Org. Chem.* **2007**, *72* (24), 9225–9230. https://doi.org/10.1021/jo701652y.

(95) Arzillo, M.; Mangiapia, G.; Pezzella, A.; Heenan, R. K.; Radulescu, A.; Paduano, L.; d'Ischia, M. Eumelanin Buildup on the Nanoscale: Aggregate Growth/Assembly and Visible Absorption Development in Biomimetic 5,6-Dihydroxyindole Polymerization. *Biomacromolecules* **2012**, *13* (8), 2379–2390. https://doi.org/10.1021/bm3006159.

(96) Bothma, J. P.; de Boor, J.; Divakar, U.; Schwenn, P. E.; Meredith, P. Device-Quality Electrically Conducting Melanin Thin Films. *Adv. Mater.* **2008**, *20* (18), 3539–3542. https://doi.org/10.1002/adma.200703141.

(97) Mostert, A. B. Melanin, the What, the Why and the How: An Introductory Review for Materials Scientists Interested in Flexible and Versatile Polymers. *Polymers* **2021**, *13* (10), 1670. https://doi.org/10.3390/polym13101670.

(98) Napolitano, A.; Pezzella, A.; Vincensi, M. R.; Prota, G. Oxidative Degradation of Melanins to Pyrrole Acids: A Model Study. *Tetrahedron* **1995**, *51* (20), 5913–5920. https://doi.org/10.1016/0040-4020(95)00259-B.

(99) Bloisi, F.; Pezzella, A.; Barra, M.; Alfè, M.; Chiarella, F.; Cassinese, A.; Vicari, L. Effect of Substrate Temperature on MAPLE Deposition of Synthetic Eumelanin Films. *Appl. Phys. A* **2011**, *105* (3), 619–627. https://doi.org/10.1007/s00339-011-6603-x.

(100) Stark, K. B.; Gallas, J. M.; Zajac, G. W.; Golab, J. T.; Gidanian, S.; McIntire, T.; Farmer, P. J. Effect of Stacking and Redox State on Optical Absorption Spectra of Melanins−Comparison of Theoretical and Experimental Results. *J. Phys. Chem. B* **2005**, *109* (5), 1970–1977. https://doi.org/10.1021/jp046710z.

(101) Pezzella, A.; Barra, M.; Musto, A.; Navarra, A.; Alfè, M.; Manini, P.; Parisi, S.; Cassinese, A.; Criscuolo, V.; d'Ischia, M. Stem Cell-Compatible Eumelanin Biointerface Fabricated by Chemically Controlled Solid State Polymerization. *Mater. Horiz.* **2015**, *2* (2), 212–220. https://doi.org/10.1039/C4MH00097H.

(102) Salomäki, M.; Tupala, M.; Parviainen, T.; Leiro, J.; Karonen, M.; Lukkari, J. Preparation of Thin Melanin-Type Films by Surface-Controlled Oxidation. *Langmuir* **2016**, *32* (16), 4103–4112. https://doi.org/10.1021/acs.langmuir.6b00402.

(103) Migliaccio, L.; Manini, P.; Altamura, D.; Giannini, C.; Tassini, P.; Maglione, M. G.; Minarini, C.; Pezzella, A. Evidence of Unprecedented High Electronic Conductivity in Mammalian Pigment Based Eumelanin Thin Films After Thermal Annealing in Vacuum. *Front. Chem.* **2019**, *7*, 162. https://doi.org/10.3389/fchem.2019.00162.

(104) Wünsche, J.; Deng, Y.; Kumar, P.; Di Mauro, E.; Josberger, E.; Sayago, J.; Pezzella, A.; Soavi, F.; Cicoira, F.; Rolandi, M.; Santato, C. Protonic and Electronic Transport in Hydrated Thin Films of the Pigment Eumelanin. *Chem. Mater.* **2015**, *27* (2), 436–442. https://doi.org/10.1021/cm502939r.

(105) Mostert, A. B.; Powell, B. J.; Pratt, F. L.; Hanson, G. R.; Sarna, T.; Gentle, I. R.; Meredith, P. Role of Semiconductivity and Ion Transport in the Electrical Conduction of Melanin. *Proc. Natl. Acad. Sci.* **2012**, *109* (23), 8943–8947. https://doi.org/10.1073/pnas.1119948109.

(106) Mostert, A. B.; Rienecker, S. B.; Sheliakina, M.; Zierep, P.; Hanson, G. R.; Harmer, J. R.; Schenk, G.; Meredith, P. Engineering Proton Conductivity in Melanin Using Metal Doping. *J. Mater. Chem. B* **2020**, *8* (35), 8050–8060. https://doi.org/10.1039/D0TB01390K.

(107) Di Capua, R.; Gargiulo, V.; Alfè, M.; De Luca, G. M.; Skála, T.; Mali, G.; Pezzella, A. Eumelanin Graphene-Like Integration: The Impact on Physical Properties and Electrical Conductivity. *Front. Chem.* **2019**, *7*, 121. https://doi.org/10.3389/fchem.2019.00121.

(108) Mihai, I.; Addiégo, F.; Del Frari, D.; Bour, J.; Ball, V. Associating Oriented Polyaniline and Eumelanin in a Reactive Layer-by-Layer Manner: Composites with High Electrical Conductivity. *Colloids Surf. Physicochem. Eng. Asp.* **2013**, *434*, 118–125. https://doi.org/10.1016/j.colsurfa.2013.05.028.

(109) Gargiulo, V.; Alfè, M.; Capua, R. D.; Togna, A. R.; Cammisotto, V.; Fiorito, S.; Musto, A.; Navarra, A.; Parisi, S.; Pezzella, A. Supplementing π-Systems: Eumelanin and Graphene-like Integration towards Highly Conductive Materials for the Mammalian Cell Culture Bio-Interface. *J. Mater. Chem. B* **2015**, *3* (25), 5070–5079. https://doi.org/10.1039/C5TB00343A.

(110) Migliaccio, L.; Aprano, S.; Iannuzzi, L.; Maglione, M. G.; Tassini, P.; Minarini, C.; Manini, P.; Pezzella, A. Eumelanin-PEDOT:PSS Complementing En Route to Mammalian-Pigment-Based Electrodes: Design and Fabrication of an ITO-Free Organic Light-Emitting Device. *Adv. Electron. Mater.* **2017**, *3* (5), 1600342. https://doi.org/10.1002/aelm.201600342.

(111) Salomäki, M.; Räsänen, M.; Leiro, J.; Huti, T.; Tenho, M.; Lukkari, J.; Kankare, J. Oxidative Inorganic Multilayers for Polypyrrole Film Generation. *Adv. Funct. Mater.* **2010**, *20* (13), 2140–2147. https://doi.org/10.1002/adfm.200902412.

(112) Salomäki, M.; Myllymäki, O.; Hätönen, M.; Savolainen, J.; Lukkari, J. Layer-by-Layer Assembled Oxidative Films as General Platform for Electrodeless Formation of Conducting Polymers. *ACS Appl. Mater. Interfaces* **2014**, *6* (4), 2325–2334. https://doi.org/10.1021/am404342b.

(113) Salomäki, M.; Kauppila, J.; Kankare, J.; Lukkari, J. Oxidative Layer-By-Layer Multilayers Based on Metal Coordination: Influence of Intervening Graphene Oxide Layers. *Langmuir* **2018**, *34* (44), 13171–13182. https://doi.org/10.1021/acs.langmuir.8b02784.

(114) Decher, G. Fuzzy Nanoassemblies: Toward Layered Polymeric Multicomposites. *Science* **1997**, *277* (5330), 1232–1237. https://doi.org/10.1126/science.277.5330.1232.

(115) Lavalle, P.; Vivet, V.; Jessel, N.; Decher, G.; Voegel, J.-C.; Mesini, P. J.; Schaaf, P. Direct Evidence for Vertical Diffusion and Exchange Processes of Polyanions and Polycations in

Polyelectrolyte Multilayer Films. *Macromolecules* **2004**, *37* (3), 1159–1162. https://doi.org/10.1021/ma035326h.

(116) Merrill, M. H.; Sun, C. T. Fast, Simple and Efficient Assembly of Nanolayered Materials and Devices. *Nanotechnology* **2009**, *20* (7), 075606. https://doi.org/10.1088/0957-4484/20/7/075606.

(117) Gittleson, F. S.; Kohn, D. J.; Li, X.; Taylor, A. D. Improving the Assembly Speed, Quality, and Tunability of Thin Conductive Multilayers. *ACS Nano* **2012**, *6* (5), 3703–3711. https://doi.org/10.1021/nn204384f.

(118) Salomäki, M.; Peltonen, T.; Kankare, J. Multilayer Films by Spraying on Spinning Surface — Best of Both Worlds. *Thin Solid Films* **2012**, *520* (17), 5550–5556. https://doi.org/10.1016/j.tsf.2012.04.055.

(119) Salomäki, M.; Jaakkola, O.; Hirvonen, S.-P.; Tenhu, H.; Kvarnström, C. Highly Controllable Ambient Atmosphere Spray Deposition of Water Dispersible poly(benzimidazobenzophenanthroline) Films. *Synth. Met.* **2018**, *245*, 144–150. https://doi.org/10.1016/j.synthmet.2018.08.022.

(120) Larocca, N. M.; Filho, R. B.; Pessan, L. A. Influence of Layer-by-Layer Deposition Techniques and Incorporation of Layered Double Hydroxides (LDH) on the Morphology and Gas Barrier Properties of Polyelectrolytes Multilayer Thin Films. *Surf. Coat. Technol.* **2018**, *349*, 1–12. https://doi.org/10.1016/j.surfcoat.2018.05.030.

(121) Gittleson, F. S.; Hwang, D.; Ryu, W.-H.; Hashmi, S. M.; Hwang, J.; Goh, T.; Taylor, A. D. Ultrathin Nanotube/Nanowire Electrodes by Spin–Spray Layer-by-Layer Assembly: A Concept for Transparent Energy Storage. *ACS Nano* **2015**, *9* (10), 10005–10017. https://doi.org/10.1021/acsnano.5b03578.

(122) Schlenoff, J. B.; Dubas, S. T.; Farhat, T. Sprayed Polyelectrolyte Multilayers. *Langmuir* **2000**, *16* (26), 9968–9969. https://doi.org/10.1021/la001312i.

(123) Izquierdo, A.; Ono, S. S.; Voegel, J.-C.; Schaaf, P.; Decher, G. Dipping versus Spraying: Exploring the Deposition Conditions for Speeding Up Layer-by-Layer Assembly. *Langmuir* **2005**, *21* (16), 7558–7567. https://doi.org/10.1021/la047407s.

(124) Krogman, K. C.; Zacharia, N. S.; Schroeder, S.; Hammond, P. T. Automated Process for Improved Uniformity and Versatility of Layer-by-Layer Deposition. *Langmuir* **2007**, *23* (6), 3137–3141. https://doi.org/10.1021/la063085b.

(125) Cho, J.; Char, K.; Hong, J.-D.; Lee, K.-B. Fabrication of Highly Ordered Multilayer Films Using a Spin Self-Assembly Method. *Adv. Mater.* **2001**, *13* (14), 1076–1078. https://doi.org/10.1002/1521-4095(200107)13:14<1076::AID-ADMA1076>3.0.CO;2-M.

(126) Richardson, J. J.; Björnmalm, M.; Caruso, F. Technology-Driven Layer-by-Layer Assembly of Nanofilms. *Science* **2015**, *348* (6233), aaa2491. https://doi.org/10.1126/science.aaa2491.

(127) Jonas, F.; Schrader, L. Conductive Modifications of Polymers with Polypyrroles and Polythiophenes. *Synth. Met.* **1991**, *41* (3), 831–836. https://doi.org/10.1016/0379-6779(91)91506-6.

(128) Jin Bae, E.; Hun Kang, Y.; Jang, K.-S.; Yun Cho, S. Enhancement of Thermoelectric Properties of PEDOT:PSS and Tellurium-PEDOT:PSS Hybrid Composites by Simple Chemical Treatment. *Sci. Rep.* **2016**, *6* (1), 18805. https://doi.org/10.1038/srep18805.

(129) Winther-Jensen, B.; Breiby, D. W.; West, K. Base Inhibited Oxidative Polymerization of 3,4-Ethylenedioxythiophene with Iron(III)Tosylate. *Synth. Met.* **2005**, *152* (1–3), 1–4. https://doi.org/10.1016/j.synthmet.2005.07.085.

(130) Winther-Jensen, B.; West, K. Vapor-Phase Polymerization of 3,4-Ethylenedioxythiophene: A Route to Highly Conducting Polymer Surface Layers. *Macromolecules* **2004**, *37* (12), 4538–4543. https://doi.org/10.1021/ma049864l.

(131) Lee, S.; Gleason, K. K. Enhanced Optical Property with Tunable Band Gap of Cross-Linked PEDOT Copolymers via Oxidative Chemical Vapor Deposition. *Adv. Funct. Mater.* **2015**, *25* (1), 85–93. https://doi.org/10.1002/adfm.201402924.

(132) Li, J.; Zhang, M.; Liu, J.; Ma, Y. Effect of Attached Peroxyacid on Liquid Phase Depositional Polymerization of EDOT over PI Film with Adsorbed Ferric Chloride. *Synth. Met.* **2014**, *198*, 161–166. https://doi.org/10.1016/j.synthmet.2014.10.008.

(133) Li, J.; Ma, Y. In-Situ Synthesis of Transparent Conductive PEDOT Coating on PET Foil by Liquid Phase Depositional Polymerization of EDOT. *Synth. Met.* **2016**, *217*, 185–188. https://doi.org/10.1016/j.synthmet.2016.03.007.

(134) Metsik, J.; Timusk, M.; Šutka, A.; Mooste, M.; Tammeveski, K.; Mäeorg, U. In Situ Investigation of Poly(3,4-ethylenedioxythiophene) Film Growth during Liquid Phase Deposition Polymerization. *Thin Solid Films* **2018**, *653*, 274–283. https://doi.org/10.1016/j.tsf.2018.02.019.

(135) Li, J.-X.; Ma, Y.-X. Study on Fabricating PEDOT Electrodes by Liquid Phase Depositional Polymerization of EDOT and Direct Patterning with 172 Nm Vacuum Ultraviolet Radiation. *ACS Appl. Energy Mater.* **2018**, *1* (1), 134–142. https://doi.org/10.1021/acsaem.7b00031.

(136) *Singlet Oxygen: Applications in Biosciences and Nanosciences*; Nonell, S., Flors, C., Eds.; Comprehensive Series in Photochemical & Photobiological Sciences; Royal Society of Chemistry: Cambridge, 2016; Vol. 1. https://doi.org/10.1039/9781782622208.

(137) Miller, D. Transition Metals as Catalysts of "Autoxidation" Reactions. *Free Radic. Biol. Med.* **1990**, *8* (1), 95–108. https://doi.org/10.1016/0891-5849(90)90148-C.

(138) Koppenol, W. H.; Stanbury, D. M.; Bounds, P. L. Electrode Potentials of Partially Reduced Oxygen Species, from Dioxygen to Water. *Free Radic. Biol. Med.* **2010**, *49* (3), 317–322. https://doi.org/10.1016/j.freeradbiomed.2010.04.011.

(139) Bertini, I.; Gray, H. B.; Lippard, S. J.; Valentine, J. S. *Bioinorganic Chemistry*; University Science Books: Mill Valley, California, 1994.

(140) Wyler, H.; Chiovini, J. Die Synthese von Cyclodopa (Leukodopachrom). *Helv. Chim. Acta* **1968**, *51* (6), 1476–1494. https://doi.org/10.1002/hlca.19680510636.

(141) Land, E. J.; Ito, S.; Wakamatsu, K.; Riley, P. A. Rate Constants for the First Two Chemical Steps of Eumelanogenesis. *Pigment Cell Res.* **2003**, *16* (5), 487–493. https://doi.org/10.1034/j.1600-0749.2003.00082.x.

(142) Bisaglia, M.; Mammi, S.; Bubacco, L. Kinetic and Structural Analysis of the Early Oxidation Products of Dopamine. *J. Biol. Chem.* **2007**, *282* (21), 15597–15605. https://doi.org/10.1074/jbc.M610893200.

(143) Thompson, A.; Land, E. J.; Chedekel, M. R.; Subbarao, K. V.; Truscott, T. G. A Pulse Radiolysis Investigation of the Oxidation of the Melanin Precursors 3,4-Dihydroxyphenylalanine (Dopa) and the Cysteinyldopas. *Biochim. Biophys. Acta BBA - Gen. Subj.* **1985**, *843* (1–2), 49–57. https://doi.org/10.1016/0304-4165(85)90048-0.

(144) Pham, A. N.; Waite, T. D. Cu(II)-Catalyzed Oxidation of Dopamine in Aqueous Solutions: Mechanism and Kinetics. *J. Inorg. Biochem.* **2014**, *137*, 74–84. https://doi.org/10.1016/j.jinorgbio.2014.03.018.

(145) Sánchez-Rivera, A. E.; Corona-Avendaño, S.; Alarcón-Angeles, G.; Rojas-Hernández, A.; Ramírez-Silva, M. T.; Romero-Romo, M. A. Spectrophotometric Study on the Stability of Dopamine and the Determination of Its Acidity Constants. *Spectrochim. Acta. A. Mol. Biomol. Spectrosc.* **2003**, *59* (13), 3193–3203. https://doi.org/10.1016/S1386-1425(03)00138-0.

(146) Young, T. E.; Babbitt, B. W. Electrochemical Study of the Oxidation of .Alpha.-Methyldopamine, .Alpha.-Methylnoradrenaline, and Dopamine. *J. Org. Chem.* **1983**, *48* (4), 562–566. https://doi.org/10.1021/jo00152a029.

(147) Linert, W.; Herlinger, E.; Jameson, R. F.; Kienzl, E.; Jellinger, K.; Youdim, M. B. H. Dopamine, 6-Hydroxydopamine, Iron, and Dioxygen — Their Mutual Interactions and Possible Implication in the Development of Parkinson's Disease. *Biochim. Biophys. Acta BBA - Mol. Basis Dis.* **1996**, *1316* (3), 160–168. https://doi.org/10.1016/0925-4439(96)00020-8.

(148) Bernsmann, F.; Ball, V.; Addiego, F.; Ponche, A.; Michel, M.; Gracio, J. J. de A.; Toniazzo, V.; Ruch, D. Dopamine−Melanin Film Deposition Depends on the Used Oxidant and Buffer Solution. *Langmuir* **2011**, *27* (6), 2819–2825. https://doi.org/10.1021/la104981s.

(149) Ball, V.; Gracio, J.; Vila, M.; Singh, M. K.; Metz-Boutigue, M.-H.; Michel, M.; Bour, J.; Toniazzo, V.; Ruch, D.; Buehler, M. J. Comparison of Synthetic Dopamine–Eumelanin Formed in the Presence of Oxygen and Cu^{2+} Cations as Oxidants. *Langmuir* **2013**, *29* (41), 12754–12761. https://doi.org/10.1021/la4029782.

(150) Yun, D.-J.; Chung, J.; Kim, S. H.; Kim, Y.; Seol, M.; Chung, J.; Park, S.-H. Study on the Molecular Distribution of Organic Composite Films by Combining Photoemission Spectroscopy with Argon Gas Cluster Ion Beam Sputtering. *J. Mater. Chem. C* **2015**, *3* (2), 276–282. https://doi.org/10.1039/C4TC01684J.

(151) Paulin, J. V.; McGettrick, J. D.; Graeff, C. F. O.; Mostert, A. B. Melanin System Composition Analyzed by XPS Depth Profiling. *Surf. Interfaces* **2021**, *24*, 101053. https://doi.org/10.1016/j.surfin.2021.101053.

(152) de Jager, H.-J.; Heyns, A. M. Kinetics of Acid-Catalyzed Hydrolysis of a Polyphosphate in Water. *J. Phys. Chem. A* **1998**, *102* (17), 2838–2841. https://doi.org/10.1021/jp9730252.

(153) Watanabe, M.; Sato, S.; Saito, H. The Mechanism of the Hydrolysis of Condensed Phosphates. II. The Mechanism of the Degradation of Long-Chain Polyphosphates. *Bull. Chem. Soc. Jpn.* **1975**, *48* (3), 896–898. https://doi.org/10.1246/bcsj.48.896.

(154) van Steveninck, J. The Influence of Metal Ions on the Hydrolysis of Polyphosphates*. *Biochemistry* **1966**, *5* (6), 1998–2002. https://doi.org/10.1021/bi00870a030.

(155) Kassamakov, I. Vl.; Seppänen, H. O.; Oinonen, M. J.; Hæggström, E. O.; Österberg, J. M.; Aaltonen, J. P.; Saarikko, H.; Radivojevic, Z. P. Scanning White Light Interferometry in Quality Control of Single-Point Tape Automated Bonding. *Microelectron. Eng.* **2007**, *84* (1), 114–123. https://doi.org/10.1016/j.mee.2006.08.013.

(156) Nabilah Azman, N. H.; Lim, H. N.; Sulaiman, Y. Effect of Electropolymerization Potential on the Preparation of PEDOT/Graphene Oxide Hybrid Material for Supercapacitor Application. *Electrochimica Acta* **2016**, *188*, 785–792. https://doi.org/10.1016/j.electacta.2015.12.019.

(157) Mohd Abdah, M. A. A.; Zubair, N. A.; Azman, N. H. N.; Sulaiman, Y. Fabrication of PEDOT Coated PVA-GO Nanofiber for Supercapacitor. *Mater. Chem. Phys.* **2017**, *192*, 161–169. https://doi.org/10.1016/j.matchemphys.2017.01.058.

(158) Mao, X.; Yang, W.; He, X.; Chen, Y.; Zhao, Y.; Zhou, Y.; Yang, Y.; Xu, J. The Preparation and Characteristic of Poly (3,4-ethylenedioxythiophene)/Reduced Graphene Oxide Nanocomposite and Its Application for Supercapacitor Electrode. *Mater. Sci. Eng. B* **2017**, *216*, 16–22. https://doi.org/10.1016/j.mseb.2016.10.002.

(159) Chen, Y.; Xu, J.; Mao, Y.; Yang, Y.; Yang, W.; Li, S. Electrochemical Performance of Graphene-Polyethylenedioxythiophene Nanocomposites. *Mater. Sci. Eng. B* **2013**, *178* (17), 1152–1157. https://doi.org/10.1016/j.mseb.2013.06.016.

(160) Taberna, P. L.; Simon, P.; Fauvarque, J. F. Electrochemical Characteristics and Impedance Spectroscopy Studies of Carbon-Carbon Supercapacitors. *J. Electrochem. Soc.* **2003**, *150* (3), A292. https://doi.org/10.1149/1.1543948.

(161) Bueno, P. R.; Mizzon, G.; Davis, J. J. Capacitance Spectroscopy: A Versatile Approach To Resolving the Redox Density of States and Kinetics in Redox-Active Self-Assembled Monolayers. *J. Phys. Chem. B* **2012**, *116* (30), 8822–8829. https://doi.org/10.1021/jp303700f.

(162) Bueno, P. R.; Varela, J. A.; Longo, E. Admittance and Dielectric Spectroscopy of Polycrystalline Semiconductors. *J. Eur. Ceram. Soc.* **2007**, *27* (13–15), 4313–4320. https://doi.org/10.1016/j.jeurceramsoc.2007.02.155.

(163) Amatore, C.; Maisonhaute, E. When Voltammetry Reaches Nanoseconds. *Anal. Chem.* **2005**, *77* (15), 303 A-311 A. https://doi.org/10.1021/ac053430m.

(164) Chmiola, J.; Yushin, G.; Gogotsi, Y.; Portet, C.; Simon, P.; Taberna, P. L. Anomalous Increase in Carbon Capacitance at Pore Sizes Less Than 1 Nanometer. *Science* **2006**, *313* (5794), 1760–1763. https://doi.org/10.1126/science.1132195.

(165) Kumar, A.; Kumar, N.; Sharma, Y.; Leu, J.; Tseng, T. Y. Synthesis of Free-Standing Flexible RGO/MWCNT Films for Symmetric Supercapacitor Application. *Nanoscale Res. Lett.* **2019**, *14* (1), 266. https://doi.org/10.1186/s11671-019-3100-1.

(166) Cougnon, C.; Lebègue, E.; Pognon, G. Impedance Spectroscopy Study of a Catechol-Modified Activated Carbon Electrode as Active Material in Electrochemical Capacitor. *J. Power Sources* **2015**, *274*, 551–559. https://doi.org/10.1016/j.jpowsour.2014.10.091.

(167) Lee, H. U.; Jin, J.-H.; Kim, S. W. Effect of Gel Electrolytes on the Performance of a Minimized Flexible Micro-Supercapacitor Based on Graphene/PEDOT Composite Using Pen Lithography. *J. Ind. Eng. Chem.* **2019**, *71*, 184–190. https://doi.org/10.1016/j.jiec.2018.11.021.

(168) Yan, D.; Li, Y.; Liu, Y.; Zhuo, R.; Geng, B.; Wu, Z.; Wang, J.; Ren, P.; Yan, P. Design and Influence of Mass Ratio on Supercapacitive Properties of Ternary Electrode Material Reduced Graphene Oxide@MnO_2@ Poly(3,4-ethylenedioxythiophene)-Poly(styrene sulfonate). *Electrochimica Acta* **2015**, *169*, 317–325. https://doi.org/10.1016/j.electacta.2015.04.078.

(169) Gonçalves, R.; Pereira, E. C.; Marchesi, L. F. The Overoxidation of Poly(3-hexylthiophene) (P3HT) Thin Film: CV and EIS Measurements. *Int. J. Electrochem. Sci.* **2017**, 1983–1991. https://doi.org/10.20964/2017.03.44.

(170) Sivaraman, P.; Bhattacharrya, A. R.; Mishra, S. P.; Thakur, A. P.; Shashidhara, K.; Samui, A. B. Asymmetric Supercapacitor Containing Poly(3-methyl thiophene)-Multiwalled Carbon Nanotubes Nanocomposites and Activated Carbon. *Electrochimica Acta* **2013**, *94*, 182–191. https://doi.org/10.1016/j.electacta.2013.01.123.

(171) Lagoutte, S.; Aubert, P.-H.; Pinault, M.; Tran-Van, F.; Mayne-L'Hermite, M.; Chevrot, C. Poly(3-methylthiophene)/Vertically Aligned Multi-Walled Carbon Nanotubes: Electrochemical Synthesis, Characterizations and Electrochemical Storage Properties in Ionic Liquids. *Electrochimica Acta* **2014**, *130*, 754–765. https://doi.org/10.1016/j.electacta.2014.03.097.

(172) Mathis, T. S.; Kurra, N.; Wang, X.; Pinto, D.; Simon, P.; Gogotsi, Y. Energy Storage Data Reporting in Perspective—Guidelines for Interpreting the Performance of Electrochemical Energy Storage Systems. *Adv. Energy Mater.* **2019**, *9* (39), 1902007. https://doi.org/10.1002/aenm.201902007.

(173) Mei, B.-A.; Lau, J.; Lin, T.; Tolbert, S. H.; Dunn, B. S.; Pilon, L. Physical Interpretations of Electrochemical Impedance Spectroscopy of Redox Active Electrodes for Electrical Energy Storage. *J. Phys. Chem. C* **2018**, *122* (43), 24499–24511. https://doi.org/10.1021/acs.jpcc.8b05241.

(174) Clark, M. B.; Gardella, J. A.; Schultz, T. M.; Patil, D. G.; Salvati, Lawrence. Solid-State Analysis of Eumelanin Biopolymers by Electron Spectroscopy for Chemical Analysis. *Anal. Chem.* **1990**, *62* (9), 949–956. https://doi.org/10.1021/ac00208a011.

(175) Il'ichev, Y. V.; Simon, J. D. Building Blocks of Eumelanin: Relative Stability and Excitation Energies of Tautomers of 5,6-Dihydroxyindole and 5,6-Indolequinone. *J. Phys. Chem. B* **2003**, *107* (29), 7162–7171. https://doi.org/10.1021/jp034702x.

(176) Pezzella, A.; Crescenzi, O.; Panzella, L.; Napolitano, A.; Land, E. J.; Barone, V.; d'Ischia, M. Free Radical Coupling of *o*-Semiquinones Uncovered. *J. Am. Chem. Soc.* **2013**, *135* (32), 12142–12149. https://doi.org/10.1021/ja4067332.

(177) Mostert, A. B. On the Free Radical Redox Chemistry of 5,6-Dihydroxyindole. *Chem. Phys.* **2021**, *546*, 111158. https://doi.org/10.1016/j.chemphys.2021.111158.

(178) Szpoganicz, B.; Gidanian, S.; Kong, P.; Farmer, P. Metal Binding by Melanins: Studies of Colloidal Dihydroxyindole-Melanin, and Its Complexation by Cu(II) and Zn(II) Ions. *J. Inorg. Biochem.* **2002**, *89* (1–2), 45–53. https://doi.org/10.1016/S0162-0134(01)00406-8.

(179) Gidanian, S.; Farmer, P. J. Redox Behavior of Melanins: Direct Electrochemistry of Dihydroxyindole-Melanin and Its Cu and Zn Adducts. *J. Inorg. Biochem.* **2002**, *89* (1–2), 54–60. https://doi.org/10.1016/S0162-0134(01)00405-6.

(180) Sofen, S. R.; Cooper, S. R.; Raymond, K. N. Crystal and Molecular Structures of Tetrakis(Catecholato)Hafnate(IV) and -Cerate(IV). Further Evidence for a Ligand Field Effect in the Structure of Tetrakis(Catecholato)Uranate(IV). *Inorg. Chem.* **1979**, *18* (6), 1611–1616. https://doi.org/10.1021/ic50196a046.

(181) Pham, T. A.; Altman, A. B.; Stieber, S. C. E.; Booth, C. H.; Kozimor, S. A.; Lukens, W. W.; Olive, D. T.; Tyliszczak, T.; Wang, J.; Minasian, S. G.; Raymond, K. N. A Macrocyclic Chelator That Selectively Binds Ln^{4+} over Ln^{3+} by a Factor of 10^{29}. *Inorg. Chem.* **2016**, *55* (20), 9989–10002. https://doi.org/10.1021/acs.inorgchem.6b00684.

(182) Gouda, A.; Soavi, F.; Santato, C. Eumelanin Electrodes in Buffered Aqueous Media at Different pH Values. *Electrochimica Acta* **2020**, *347*, 136250. https://doi.org/10.1016/j.electacta.2020.136250.

TURUN
YLIOPISTO
UNIVERSITY
OF TURKU

Painosalama Oy, Turku, Finland 2022

ISBN 978-951-29-9095-5 (PRINT)
ISBN 978-951-29-9096-2 (PDF)
ISSN 0082-7002 (Print)
ISSN 2343-3175 (Online)